The effect of the zero-field splitting ~~interaction~~ in light-induced pulsed dipolar EPR spectroscopy

Andreas Scherer, Berk Yildirim, Malte Drescher

5 Department of Chemistry and Konstanz Research School Chemical Biology, University of Konstanz, 78457 Konstanz, Germany

Correspondence to: Malte Drescher (malte.drescher@uni-konstanz.de)

Abstract. Laser-induced magnetic dipole (LaserIMD) spectroscopy ~~(LaserIMD)~~ and light-induced double electron-electron resonance (LiDEER) spectroscopy ~~(LiDEER)~~ are important techniques in the emerging field of light-induced pulsed dipolar

10 EPR spectroscopy (light-induced PDS). These techniques use the photoexcitation of a chromophore to the triplet state and measure its dipolar coupling to a neighboring electron spin, which allows the determination of distance restraints. LaserIMD and LiDEER were so far analyzed with software tools that were developed for a pair of two $S = 1/2$ spins and neglect the zero-field splitting ~~interaction~~ (ZFS) of the excited triplet. Here, we ~~show~~ explore ~~that th~~the limits of this assumption and show that the~~e~~ ZFS ~~cannot be neglected in light-induced PDS, as it has~~can have a significant~~n~~ effect on the shape of the dipolar

15 trace. For a detailed understanding of the effect of the ZFS, a theoretical description for LaserIMD and LiDEER is derived, taking into account the non-secular terms of the ZFS. Simulations based on this model show that the effect of the ZFS is not so pronounced in LiDEER for experimentally relevant conditions. However, the ZFS leads to an additional decay in the dipolar trace in LaserIMD. This ~~effect~~ decay is not so pronounced in Q-band but can be quite noticeable for lower magnetic field ~~like~~ strengths in X-band. Experimentally recorded LiDEER and LaserIMD data confirm these findings. ~~and~~ It is shown that ~~the~~

20 ignoring the ZFS in the data analysis of LaserIMD traces can lead to errors in the obtained modulation depths and background decays. In X-band, it is additionally possible that the obtained distance distribution is plagued by long distance artifacts. ~~is an important parameter that needs to be considered for the accurate description of light-induced PDS.~~

1 Introduction

Pulsed dipolar EPR spectroscopy (PDS) has become an important tool for nanoscale distance determination in soft matter. Its

25 applications include the structural determination of biomacromolecules like proteins (Yee et al., 2015; Yang et al., 2020; Giannoulis et al., 2020; Weickert et al., 2020; Robotta et al., 2014; Ritsch et al., 2022), DNA (Wojciechowski et al., 2015; Takeda et al., 2004; Marko et al., 2011) and RNA (Collauto et al., 2020), but also synthetic polymers (Jeschke et al., 2010) as well as nanoparticles (Hintze et al., 2015; Bücker et al., 2019). PDS measures the dipolar coupling between two spin centers within the molecule under investigation. Oftentimes, the spin centers need to be introduced as spin labels via site-directed

30 labeling, with nitroxide spin probes as the most common example (Hubbell et al., 2013; Roser et al., 2016; García-Rubio, 2020). The most common PDS technique is double electron-electron resonance ~~spectroscopy~~ (DEER, also called PELDOR)

1

spectroscopy (Milov et al., 1981, 1984; Jeschke, 2012). Here, one of the spin labels is excited by microwave pulses at an observer frequency to generate a refocused echo. The excitation of the other spin label by a pump pulse at a second frequency leads to an oscillation of the refocused echo, when the pump pulse is shifted in the time domain. The frequency of this oscillation depends on the inverse cubic distance between the spin labels r^{-3} and thus provides distance information for the molecule under investigation (Jeschke, 2012).

The recent years have seen an advent of a new type of spin label, which are in an EPR-silent singlet ground state, but can be converted transiently to a triplet state by photoexcitation and subsequent inter-system crossing (Di Valentin et al., 2014; Bertran et al., 2022a). In contrast to spin labels with a spin of $S = 1/2$ like nitroxides, these transient triplet labels are subject to an additional zero-field splitting (ZFS). It is described by the ZFS parameters D and E. By now, several ~~of these~~ transient triplet labels with different ZFS strengths have been used. ~~like~~ Examples are triphenylporphyrin (TPP)~~s~~ ($D = 1159$ MHz, $E = -238$ MHz) (Di Valentin et al., 2014), fullerenes ($D = 342$ MHz, $E = -2$ MHz) (Wasielewski et al., 1991; Krumacheva et al., 2019; Timofeev et al., 2022), Rose Bengal ($D = 3671$ MHz, $E = -319$ MHz), Eosin Y ($D = 2054$ MHz, $E = -585$ MHz)~~, and~~ Atto Thio12 ($D = 1638$ MHz, $E = -375$ MHz) (Serrer et al., 2019; Williams et al., 2020) and Erythrosin B ($D = 3486$ MHz, $E = -328$ MHz) (Bertran et al., 2022b) ~~have been used~~. The most common PDS techniques for transient triplet labels are light-induced DEER (LiDEER) and laser-induced magnetic dipole (LaserIMD) spectroscopy ~~(LaserIMD)~~ (Di Valentin et al., 2014; Hintze et al., 2016). They both allow the determination of distances between one permanent spin label and one transient triplet label. LiDEER is a modification of DEER with an additional laser flash preceding the microwave pulses (see Figure 1a). ~~The transient triplet label is observed and t~~ The permanent spin is excited by the pump pulse, because it typically has an EPR spectrum that is narrower than the one of the transient triplet label, which gives higher modulation depths. The transient triplet label is observed, because despite its broader EPR spectrum it is still possible to generate strong echoes, because the photoexcitation of the transient triplet label typically leads to a high spin polarization ~~(Fig. 1a)~~ (Di Valentin et al., 2014). In LaserIMD, on the other ~~side~~hand, the permanent spin label is observed. During the evolution of the observer spin, the transient triplet label is excited by a laser flash (see Figure 1~~Fig. 1~~b). The induced transition from the singlet to the triplet state has the equivalent effect as the microwave pump pulse in DEER and results in an oscillation of the echo of the observer spin. An advantage of LaserIMD is that, in contrast to DEER, the bandwidth of the laser excitation is neither limited by the width of the EPR spectrum of the pump spin nor the resonator bandwidth. This gives ~~a~~ virtually infinite excitation bandwidths and promises high modulation depths also in cases where the microwave excitation bandwidth is smaller than the EPR spectra of the invoked spins (Scherer et al., 2022).
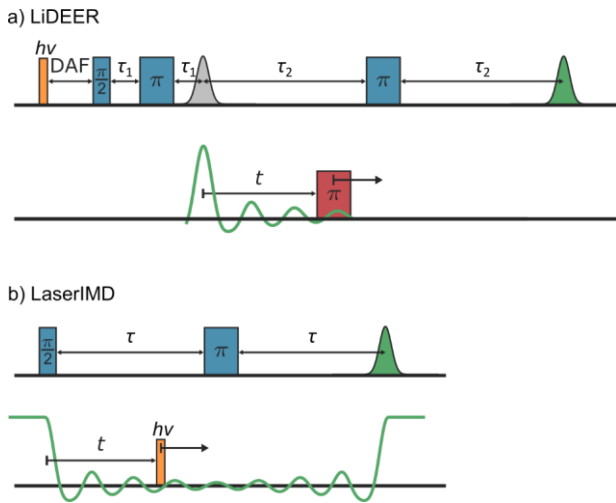
Figure 1: The pulse sequences of a) LiDEER and b) LaserIMD. The observed green echoes are modulated when the pump pulse (LiDEER) or laser flash (LaserIMD) is shifted in the time domain.

In previous works, LaserIMD and LiDEER data were analyzed under the assumption that ~~contributions from~~ the ~~zero-field splitting interaction (ZFS)~~ZFS of the transient triplet label can be ignored (Di Valentin et al., 2014; Hintze et al., 2016; Bieber et al., 2018; Dal Farra et al., 2019a; Krumkacheva et al., 2019).~~, which means~~ Under this assumption ~~that~~ the dipolar traces of LaserIMD and LiDEER have the same shape as ~~those~~those ~~for~~of ~~a~~DEER on a label pair with two $S = 1/2$ spins ~~pair~~. However, as is shown below,~~This is~~ this assumption is only correct if all spin-spin interactions are much smaller than the Zeeman-interaction with the external magnetic field. Then, all non-secular terms in the Hamiltonian can be dropped (Manukovsky et al., 2017). ~~Most PDS experiments like e.g. nitroxide-nitroxide DEER can be analyzed with this assumption (Jeschke et al., 2006; Fábregas Ibáñez et al., 2020).~~ The excited triplet state of transient triplet labels with a total spin of $S = 1$, however, can be subject to a strong ZFS, reaching values over 1 GHz in many cases (Di Valentin et al., 2014; Williams et al., 2020). For other high-spin labels like Gd^{III} or high-spin Fe^{III}, it is already known that the ZFS can have an effect on the recorded dipolar trace and that it has to be included in the data-analysis routine, if art~~e~~ifacts in the distance shall be avoided (Maryasov et al., 2006; Dalaloyan et al., 2015; Abdullin et al., 2019).

Here, we set out to investigate the effect of the ZFS in light-induced PDS. Therefore, we are going to derive a theoretical description for light-induced PDS taking the $S = 1$ spin state and ZFS of the triplet state into account. Section 3 will report about the materials and methods used. In section 4, the theoretical model will be used for numerical simulations of LaserIMD and time-domain simulations were performed for LiDEER. It will be shown that in both methods, but particularly in LaserIMD,

the effect of the ZFS can result in significant differences in the dipolar traces compared to the $S = 1/2$ case where the ZFS is ignored. In section 5, experimental LaserIMD and LiDEER traces are shown and the influence of the ZFS is discussed by comparing the model with the experimental data.

2 Theoretical derivation

2.1 DEER

For the analysis of DEER data, one typically uses the assumption that both spins are of $S = 1/2$ nature and the system is in high-field and weak-coupling limit so that all pseudo- and non-secular parts of the spin Hamiltonian can be dropped (Jeschke et al., 2006; Worswick et al., 2018; Fábregas Ibáñez et al., 2020). In this case, there are two coherence transfer pathways that contribute to the DEER signal; one where the pump spin is flipped from the state with $m_S = +1/2$ to $m_S = -1/2$, and the one where it is flipped from $m_S = -1/2$ to $m_S = +1/2$. The frequency of the dipolar oscillation of the refocused echo for the two coherence transfer pathways is (Sweger et al., 2022):

$$\omega_{\mathrm{DEER}, +\frac{1}{2} \to -\frac{1}{2}} = \left(3\cos(\beta_{\mathrm{dip}})^2 - 1\right)\omega_{\mathrm{dip}}, \tag{1}$$

$$\omega_{\mathrm{DEER}, -\frac{1}{2} \to +\frac{1}{2}} = -\left(3\cos(\beta_{\mathrm{dip}})^2 - 1\right)\omega_{\mathrm{dip}}. \tag{2}$$

Here, β_{dip} is the angle between the dipolar coupling vector and the external magnetic field and ω_{dip} is the dipolar coupling in radial frequency units. It depends on the distance r between the two labels (Pannier et al., 2000; Schweiger and Jeschke, 2001; Jeschke, 2012):

$$\omega_{\mathrm{dip}} = \frac{\mu_{\mathrm{B}}^2 g_1 g_2}{\hbar}\frac{1}{r^3}, \tag{3}$$

With the Bohr-magneton μ_{B}, the reduced Plank constant $\hbar$, and the g-values g_1 and g_2 of the two spin labels. In experiments one typically measures powder samples, thus molecules with all orientations with respect to the external field contribute to the signal, and the weighted integral over all angles β_{dip} must be taken (Pake, 1948; Milov et al., 1998). In the high-temperature limit, which is often fulfilled in experiments, the population of the spin states with $m_S = +1/2$ to $m_S = -1/2$ is virtually identical and therefore both coherence transfer pathways contribute equally to the signal (Marko et al., 2013). In this case the integral over all orientations is:

$$S_{\mathrm{DEER}}(t, r) = \int_0^{\pi/2} \mathrm{d}\beta_{\mathrm{dip}} \sin(\beta_{\mathrm{dip}}) \cos\left(t\left(3\cos(\beta_{\mathrm{dip}})^2 - 1\right)\omega_{\mathrm{dip}}(r)\right) \tag{4}$$

Here, t is the time at which the pump pulse flips the pump spins. Due to a limited excitation bandwidth and pulse imperfections not all spins can be excited by the pump pulse, therefore a part of the signal is not modulated:

4

Formatiert: Schriftfarbe: Rot

$$F_{\text{DEER}}(t,r) = \lambda S_{\text{DEER}}(t,r) + (1-\lambda), \tag{5}$$

where the modulation depth λ depends on the fraction of excited pump spins. The experimental signal is the product of this intramolecular contribution $F_{\text{DEER}}(t,r)$ and a contribution from the intermolecular dipolar interactions $B(t)$, that is typically termed background (Jeschke, 2016). Finally, the contributions from all distances need to be included by integrating over the distance distribution $P(r)$:

$$V_{\text{DEER}}(t) = \int \mathrm{d}r K_{\text{DEER}}(t,r) P(r) = \int \mathrm{d}r B(t) F_{\text{DEER}}(t,r) P(r). \tag{6}$$

5 The kernel $K_{\text{DEER}}(t,r)$ describes the relation between the distance distribution and the measured dipolar trace in DEER. In a sample with a homogenous distribution of spins, the background function can be obtained by integrating over all dipolar interactions within the sample, which results in (Hu and Hartmann, 1974):

$$B(t) = \exp(-k|t|). \tag{7}$$

The decay constant k is proportional to the spin concentration and modulation depth (Hu and Hartmann, 1974). By inverting Eq. (6), it is possible to extract the distance distribution $P(r)$ from the experimentally recorded signal $V_{\text{DEER}}(t)$. Because this

10 is an ill-posed problem, this is typically done by advanced techniques like Tikhonov regularization (Bowman et al., 2004; Jeschke et al., 2004) or neural networks (Worswick et al., 2018; Keeley et al., 2022).

2.2 LaserIMD

In LaserIMD, the spin system consists of a permanent spin label, which serves as an observer spin, and a transient triplet label, which is excited by a laser flash. In many cases, the permanent spin label is or can be assumed to be a doublet with $S_D = 1/2$.

15 Before the photoexcitation, the transient label is still in its singlet state and does therefore neither interact with the external field B, nor with the doublet S_D. The Hamiltonian thus only contains the Zeeman interaction of S_D:

$$\hat{H}_{\text{dark}} = 2\pi \nu_D \hat{S}_{D,z}, \tag{8}$$

with the Zeeman frequency $\nu_D = \frac{g_D \mu_B}{2\pi\hbar} B$, g_D the g-values of S_D, which is assumed to be isotropic. The Hamiltonian is written in units of radial frequencies. This Hamiltonian has two eigenvalues:

$$E_{+\frac{1}{2}, \text{dark}} = \frac{2\pi\nu_D}{2}, \tag{9}$$

$$E_{-\frac{1}{2}, \text{dark}} = -\frac{2\pi\nu_D}{2}. \tag{10}$$

When the laser flash excites the transient triplet label to the triplet state $S_T = 1$, the Zeeman interaction of S_T, the ZFS between

20 the two unpaired electrons that form the triplet S_T and the dipolar coupling between S_D and S_T has to be included in the Hamiltonian:

$$\hat{H} = 2\pi\nu_D\hat{S}_{D,z} + 2\pi\nu_T\hat{S}_{T,z} + \boldsymbol{S}_T \cdot \boldsymbol{D} \cdot \boldsymbol{S}_T + \boldsymbol{S}_T \cdot \boldsymbol{T} \cdot \boldsymbol{S}_D. \tag{11}$$

Here, $\nu_T = \frac{g_T\mu_B B}{2\pi\hbar}$ is the Zeeman frequency of the spin S_T with its isotropic g-value g_T. $\bar{S}_D$ and $\bar{S}_T$ represent the vectors of the Cartesian spin operators $\boldsymbol{S}_D = (\hat{S}_{D,x}, \hat{S}_{D,y}, \hat{S}_{D,z})^T$ and $\boldsymbol{S}_T = (\hat{S}_{T,x}, \hat{S}_{T,y}, \hat{S}_{T,z})^T$. The ZFS tensor $\boldsymbol{D}$ is described by the ZFS values $D = \frac{3}{2}D_z$ and $E = \frac{D_x - D_y}{2}$, where D_x, D_y and D_z are the eigenvalues of the ZFS tensor (Telser, 2017). Its orientation is described by the three Euler angles α_T, β_T and γ_T that connect the laboratory frame with the molecular frame of the transient triplet label.

5   In the point-dipole approximation, Tthe dipolar coupling tensor $\boldsymbol{T}$ is axial with its the eigenvalues being $T_x = T_y = -\omega_{dip}$ and $T_z = 2\omega_{dip}$ (Schweiger and Jeschke, 2001). Its orientation towards the external magnetic field is described by the angle β_{dip}. In the literature up to now, aIn the high-field and weak-coupling limit is typically assumed for LaserIMD, so that all non- and pseudo-secular terms were can be dropped from the Hamiltonian. The remaining secular Hamiltonian (see Eq. (S2) in S1) is already diagonal in the high-field basis with the energy levels $E^{sec}_{m_D, m_T}$, where m_D and m_T are the magnetic quantum numbers

10   of the doublet S_D and the triplet S_T. The exact expressions for the energies $E^{sec}_{m_D, m_T}$ can be found in Eq. (S4) -(S9) in S1. In LaserIMD, the initial $\frac{\pi}{2}$-pulse generates a coherence of the observer spin S_D. Before the laser excitation, the coherence evolves with a frequency of $E_{+\frac{1}{2}, dark} - E_{-\frac{1}{2}, dark} = 2\pi\nu_D$, it is not influenced by the dipolar coupling because the transient triplet label is still in a singlet state with $S_T = 0$ and $m_T = 0$. The excitation of the transient triplet label leads to three different coherence transfer pathways, depending to which manifold $m_T = 1, 0$ or -1 of the triplet the transient label is excited to. Depending on

15   the triplet state m_T, the coherence will then continue to evolve with $E^{sec}_{+\frac{1}{2}, m_T} - E^{sec}_{-\frac{1}{2}, m_T}$. The refocusing π-pulse generates an echo at the time 2τ. Due to the different frequencies before and after the excitation at a variable time t, the coherences are not completely refocused but depending on the time of the laser flash they will have gained a phase $\phi = \omega^{sec}_{m_T}t$, that depends on the LaserIMD frequency $\omega^{sec}_{m_T}$ of the corresponding triplet manifold m_T. When only the secular terms are considered in the Hamiltonian, the LaserIMD frequencies $\omega^{sec}_{m_T}$ do not dependent on the ZFS, because its secular terms cancel each other out

20   and the same expression as by (Hintze et al., 2016) are obtained:

$$\omega^{sec}_{+1} = \left(E^{sec}_{+\frac{1}{2}, +1} - E^{sec}_{-\frac{1}{2}, +1}\right) - \left(E_{+\frac{1}{2}, dark} - E_{-\frac{1}{2}, dark}\right) = \left(3\cos(\beta_{dip})^2 - 1\right)\omega_{dip}, \tag{12}$$

$$\omega^{sec}_{0} = \left(E^{sec}_{+\frac{1}{2}, 0} - E^{sec}_{-\frac{1}{2}, 0}\right) - \left(E_{+\frac{1}{2}, dark} - E_{-\frac{1}{2}, dark}\right) = 0, \tag{13}$$

$$\omega^{sec}_{-1} = \left(E^{sec}_{+\frac{1}{2}, -1} - E^{sec}_{-\frac{1}{2}, -1}\right) - \left(E_{+\frac{1}{2}, dark} - E_{-\frac{1}{2}, dark}\right) = -\left(3\cos(\beta_{dip})^2 - 1\right)\omega_{dip}. \tag{14}$$

When the transient triplet label is excited to $m_T = 1$ or $m_T = -1$, the LaserIMD frequencies in secular-approximation from Eq. (12) and (14) are identical to the DEER frequencies in Eq. (1) and (2). Here, the laser flash leads to a change in the magnetic quantum number of $\Delta m_T = \pm 1$, which is equivalent to the effect of the microwave pump pulse in DEER. In the case when the transient triplet label is excited to the state $m_T = 0$, however, the secular approximation predicts that the echo is not oscillating,

6

because -loosely spoken- there is no change in the magnetic spin quantum number of the transient triplet label, which means that the dipolar coupling is not changed. Like it is the case in DEER, the measured signal is the average over all orientations of the spin system. Whereas in DEER it is only necessary to consider the orientation of the dipolar vector, in LaserIMD the orientation of the transient triplet label must also be taken into account, therefore it is necessary to also integrate over the three corresponding Euler angles α_T, β_T and γ_T (Bak and Nielsen, 1997). In absence of orientation selection, the orientation of the dipolar vector and the transient triplet label are not correlated and the integration over the corresponding Euler angles can be done independently. This is often realized in practical applications where flexible linkers are used to attach labels to the studied molecule. As the triplet state of the transient label is reached by intersystem-crossing, the population of the three high-field triplet states $m_T = +1, 0, -1$ depends on the orientation of the transient label with respect to the external magnetic field and the populations P_x, P_y and P_z of the zero-field eigenstates of the ZFS (Rose, 1995). The contribution of the three coherence transfer pathways must be weighted by population of these high-field states; this gives (still in secular approximation) the three expressions:

$$S_{+1}^{sec}(t,r) = \frac{1}{8\pi^2} \int_0^{2\pi} d\alpha_T \int_0^{\pi} d\beta_T \sin(\beta_T) \int_0^{2\pi} d\gamma_T \left(\frac{P_z}{2} \sin^2(\beta_T) + \frac{P_x}{2} (\cos^2(\beta_T) + \sin^2(\beta_T) \sin^2(\gamma_T)) \right.$$
$$\left. + \frac{P_y}{2} (\cos^2(\beta_T) + \sin^2(\beta_T) \cos^2(\gamma_T)) \right) \int_0^{\frac{\pi}{2}} d\beta_{dip} \sin(\beta_{dip}) \exp(-i\omega_{+1}^{sec}(\beta_{dip})t), \tag{15}$$

$$S_0^{sec}(t,r) = \frac{1}{8\pi^2} \int_0^{2\pi} d\alpha_T \int_0^{\pi} d\beta_T \sin(\beta_T) \int_0^{2\pi} d\gamma_T \left(P_z \cos^2(\beta_T) + P_x \sin^2(\beta_T) \cos^2(\gamma_T) \right.$$
$$\left. + P_y \sin^2(\beta_T) \sin^2(\gamma_T) \right) \int_0^{\pi/2} d\beta_{dip} \sin(\beta_{dip}) \exp(-i\omega_0^{sec}(\beta_{dip})t), \tag{16}$$

$$S_{-1}^{sec}(t,r) = \frac{1}{8\pi^2} \int_0^{2\pi} d\alpha_T \int_0^{\pi} d\beta_T \sin(\beta_T) \int_0^{2\pi} d\gamma_T \left(\frac{P_z}{2} \sin^2(\beta_T) + \frac{P_x}{2} (\cos^2(\beta_T) + \sin^2(\beta_T) \sin^2(\gamma_T)) \right.$$
$$\left. + \frac{P_y}{2} (\cos^2(\beta_T) + \sin^2(\beta_T) \cos^2(\gamma_T)) \right) \int_0^{\frac{\pi}{2}} d\beta_{dip} \sin(\beta_{dip}) \exp(-i\omega_{-1}^{sec}(\beta_{dip})t). \tag{17}$$

Performing the integration over the orientations of the transient label α_T, β_T and γ_T and taking the sum gives (Williams et al., 2020):

$$S_{LaserIMD}^{sec}(t,r) = S_{+1}^{sec}(t,r) + S_0^{sec}(t,r) + S_{-1}^{sec}(t,r)$$
$$= \frac{2}{3} \int_0^{\pi/2} \cos(\omega_{dip}(3\cos^2(\beta_{dip}) - 1)t) \sin(\beta_{dip}) \, d\beta_{dip} + \frac{1}{3} = \frac{2}{3} S_{DEER}(t,r) + \frac{1}{3}. \tag{18}$$

In secular-approximation, the first term of the LaserIMD signal is equivalent to the trace $S_{DEER}^{sec}(t)$ (Edwards and Stoll, 2018). The second term, however, is an additional non-modulated contribution. For the final expression for the kernel $K_{LaserIMD}^{sec}(t,r)$,

the quantum yield of the triplet state is considered by an additional factor γ and the intermolecular interaction to other spins in the sample has to be considered as background $B(t)$:

$$K_{\text{LaserIMD}}^{\text{sec}}(t,r) = B(t)(\gamma S_{\text{LaserIMD}}^{\text{sec}}(t,r) + 1 - \gamma). \tag{19}$$

This can be rewritten as:

$$K_{\text{LaserIMD}}^{\text{sec}}(t,r) = B(t)(\lambda S_{\text{DEER}}(t,r) + 1 - \lambda), \tag{20}$$

with the modulation depth $\lambda = 2/3\gamma$. The only difference between LaserIMD in the secular approximation and DEER is that in LaserIMD, even for a triplet yield of $\gamma = 100\,\%$, there is coherence transfer pathway with $\Delta m_S = 0$ that does not result in a dipolar oscillation, which limits the maximum achievable modulation depth to $66.\overline{6}\,\%$. The calculations so far show that If if the secular approximation can be employed in LaserIMD, the ZFS has no effect on the LaserIMD trace and this means that it is possible to analyze experimentally recorded LaserIMD data with the same kernel that can be used for DEER. DEER and no new analysis routine needs to be implemented.

Even though in the secular approximation the ZFS has no effect in LaserIMD, it cannot be taken for granted that the non-secular terms can be ignored because the ZFS of some transient triplet labels can be quite large (Williams et al., 2020). Here, we additionally consider the terms $\hat{S}_{\text{T},z}\hat{S}_{\text{T},+} + \hat{S}_{\text{T},+}\hat{S}_{\text{T},z}$ and $\hat{S}_{\text{T},-}\hat{S}_{\text{T},z} + \hat{S}_{\text{T},-}\hat{S}_{\text{T},z}$ from the ZFS interaction and the terms $\hat{S}_{\text{D},z}\hat{S}_{\text{T},+}$ and $\hat{S}_{\text{D},z}\hat{S}_{\text{T},-}$ from the dipolar coupling. They connect the adjacent triplet states $|+1\rangle$ and $|0\rangle$ and $|0\rangle$ and $|-1\rangle$ of the triplet manifold and shift their energy in second order (Hagston and Holmes, 1980). This is illustrated in Figure 2. The details of this calculation are described in S1. For this calculation, the remaining ZFS terms $\hat{S}_{\text{T},+}^2$ and $\hat{S}_{\text{T},-}^2$ were ignored. They connect the triplet states $|+1\rangle$ and $|-1\rangle$, which have a larger energy difference than adjacent states. Therefore, the second order energy shift of $\hat{S}_{\text{T},+}^2$ and $\hat{S}_{\text{T},-}^2$ is weaker than those of the considered terms. The terms $\hat{S}_{\text{D},+}\hat{S}_{\text{T},+}, \hat{S}_{\text{D},-}\hat{S}_{\text{T},+}, \hat{S}_{\text{D},+}\hat{S}_{\text{T},-}, \hat{S}_{\text{D},-}\hat{S}_{\text{T},-}, \hat{S}_{\text{D},+}\hat{S}_{\text{T},z}$ and $\hat{S}_{\text{D},-}\hat{S}_{\text{T},z}$ of the dipolar coupling were also ignored. They connect spin states of different manifolds of the doublet spin and the corresponding energies cannot be significantly shifted by the comparably weak dipolar coupling. In Fig. 2 it is shown, how the energy levels $E_{m_{\text{D}},m_{\text{T}}}^{\text{non-sec}}$ get shifted when additional non-secular terms of the ZFS and dipolar coupling are considered. This shift was calculated by including the non-secular terms from Eq. (S3) in S1 and diagonalizing the Hamiltonian with a second-order perturbation approach (Hagston and Holmes, 1980). This is described in detail in S1. Please note that we did not consider all non-secular terms and pseudo-secular terms were also ignored. It is shown in S2 that at magnetic field strengths that are relevant for experimental conditions the included non-secular terms from Eq. (S3) are sufficient and no further distortions are to be expected by the left-out ones.

Formatiert: Rechtschreibung und Grammatik prüfen

8
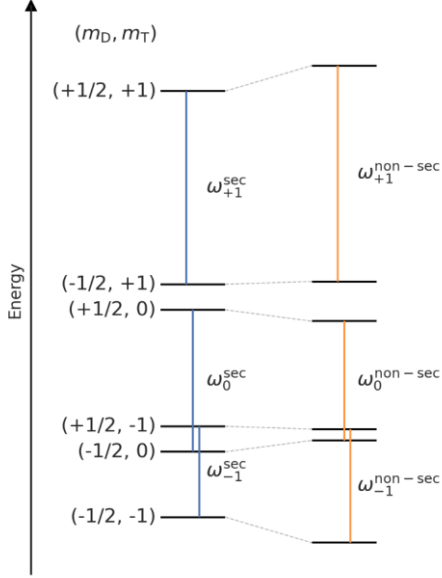
Figure 2: Energy level diagram (not to scale) after the transient triplet label has been excited to the triplet state demonstrating the shift that is induced by the non-secular terms of the ZFS and dipolar coupling from Eq. (S3). The energy levels in secular approximation are shown on the left and the levels with the non-secular terms are shown on the right. The vertical lines in blue (secular approximation) and orange (non-secular terms included) indicate the coherences of the permanent spin label that are excited during the LaserIMD pulse sequence. They are marked with the corresponding transition frequencies.

The shift of the energy levels also leads to a shift in the LaserIMD frequencies. (see S1):

$$\omega_{+1}^{\text{non-sec}} = \left(E_{+\frac{1}{2}, +1}^{\text{non-sec}} - E_{-\frac{1}{2}, +1}^{\text{non-sec}} \right) - \left(E_{+\frac{1}{2}, \text{dark}} - E_{-\frac{1}{2}, \text{dark}} \right)$$

$$= \left(\left(3\cos(\beta_{\text{dip}})^2 - 1 \right) + \delta_{\text{ZFS}} \sin(2\beta_{\text{dip}}) \right) \omega_{\text{dip}}, \tag{21}$$

$$\omega_{0}^{\text{non-sec}} = \left(E_{+\frac{1}{2}, 0}^{\text{non-sec}} - E_{-\frac{1}{2}, 0}^{\text{non-sec}} \right) - \left(E_{+\frac{1}{2}, \text{dark}} - E_{-\frac{1}{2}, \text{dark}} \right) = -2\delta_{\text{ZFS}} \sin(2\beta_{\text{dip}}) \omega_{\text{dip}}, \tag{22}$$

9

$$\omega_{-1}^{\text{non-sec}} = \left(E_{+\frac{1}{2},-1}^{\text{non-sec}} - E_{-\frac{1}{2},-1}^{\text{non-sec}} \right) - \left(E_{+\frac{1}{2},\text{dark}} - E_{-\frac{1}{2},\text{dark}} \right)$$

$$= \left(-\left(3\cos(\beta_{\text{dip}})^2 - 1 \right) + \delta_{\text{ZFS}}\sin(2\beta_{\text{dip}}) \right)\omega_{\text{dip}}, \tag{23}$$

with

$$\delta_{\text{ZFS}} = \frac{3\sin(2\beta_{\text{T}})\cos(\alpha_{\text{T}})\,D - 6\sin(\beta_{\text{T}})(\cos(\beta_{\text{T}})\cos(2\gamma_{\text{T}})\cos(\alpha_{\text{T}}) - \sin(2\gamma_{\text{T}})\sin(\alpha_{\text{T}}))E}{8\pi\nu_{\text{T}}}. \tag{24}$$

As can be seen from Eq. (21) -(23), the frequencies $\omega_{+1}^{\text{non-sec}}$ and $\omega_{-1}^{\text{non-sec}}$ are the sum of the unperturbed frequencies ω_{+1}^{sec} and ω_{-1}^{sec} and a frequency shift $\delta_{\text{ZFS}}\sin(2\beta_{\text{dip}})\omega_{\text{dip}}$, which contains the effect of the ZFS. Most notably, the coherence transfer pathway with $\Delta m_{\text{T}} = 0$ does not lead to a vanishing LaserIMD frequency as it was the case in the secular approximation.

5 Instead, we find that $\omega_0^{\text{non-sec}}$ equals twice the negative of the frequency shift that is experienced by the other two coherence transfer pathways. The frequency shift scales with δ_{ZFS} that depends on the ZFS values D and E, the Zeeman frequency of the transient triplet label ω_{T} as well as the orientation of the transient triplet label, described by α_{T}, β_{T} and γ_{T}. At a higher ZFS and a smaller magnetic field, the shift of the LaserIMD frequencies will be larger, so that larger disturbances in the LaserIMD trace can be expected in these cases.

10 The ~~integrals for the~~ powder <u>average</u> ~~are~~ <u>is</u> more complex when the non-secular terms are included, because the LaserIMD frequencies now also depend on the orientation of the transient triplet label<u>. Still assuming no orientation selection, this gives the following integrals</u>:

$$S_{+1}^{\text{non-sec}}(t,r) = \frac{1}{8\pi^2} \int_0^{2\pi} d\alpha_{\text{T}\ell} \int_0^{\pi} d\beta_t \sin(\beta_{T\ell}) \int_0^{2\pi} d\gamma_{\text{T}\ell} \left(\frac{P_z}{2}\sin^2(\beta_{\text{T}\ell}) \right.$$

$$+ \frac{P_x}{2}\left(\cos^2(\beta_{\text{T}\ell}) + \sin^2(\beta_{\text{T}\ell})\sin^2(\gamma_{\text{T}\ell}) \right)$$

$$+ \frac{P_y}{2}\left(\cos^2(\beta_{\text{T}\ell}) \right.$$

$$\left. + \sin^2(\beta_{\text{T}\ell})\cos^2(\gamma_{\text{T}\ell}) \right) \left. \vphantom{\frac{P_z}{2}} \right) \int_0^{\frac{\pi}{2}} d\beta_{\text{dip}}\sin(\beta_{\text{dip}})\exp\left(-i\omega_{+1}^{\text{non-sec}}(\alpha_{\text{T}},\beta_{\text{T}},\gamma_{\text{T}},\beta_{\text{dip}})t \right), \tag{25}$$

$$S_0^{\text{non-sec}}(t,r) = \frac{1}{8\pi^2} \int_0^{2\pi} d\alpha_{\text{T}} \int_0^{\pi} d\beta_{\text{T}}\sin(\beta_{\text{T}}) \int_0^{2\pi} d\gamma_{\text{T}}\left(P_z\cos^2(\beta_{\text{T}}) + P_x\sin^2(\beta_{\text{T}})\cos^2(\gamma_{\text{T}}) \right.$$

$$\left. + P_y\sin^2(\beta_{\text{T}})\sin^2(\gamma_{\text{T}}) \right) \int_0^{\pi/2} d\beta_{\text{dip}}\sin(\beta_{\text{dip}})\exp\left(-i\omega_0^{\text{non-sec}}(\alpha_{\text{T}},\beta_{\text{T}},\gamma_{\text{T}},\beta_{\text{dip}})t \right), \tag{26}$$

$$S_{-1}^{\text{non-sec}}(t,r) = \frac{1}{8\pi^2} \int_0^{2\pi} d\alpha_T \int_0^\pi d\beta_T \sin(\beta_t) \int_0^{2\pi} d\gamma_T \left(\frac{P_z}{2} \sin^2(\beta_T) \right.$$

$$+ \frac{P_x}{2} (\cos^2(\beta_T) + \sin^2(\beta_T)\sin^2(\gamma_T))$$

$$+ \frac{P_y}{2} (\cos^2(\beta_T)$$

$$\left. + \sin^2(\beta_T)\cos^2(\gamma_T)) \right) \int_0^{\frac{\pi}{2}} d\beta_{\text{dip}} \sin(\beta_{\text{dip}}) \exp\left(-i\omega_{-1}^{\text{non-sec}}(\alpha_T,\beta_T,\gamma_T,\beta_{\text{dip}})t\right).$$

(27)

The sum over these terms gives the final intramolecular contribution in LaserIMD.

$$S_{\text{LaserIMD}}^{\text{non-sec}}(t) = S_{+1}^{\text{non-sec}}(t) + S_0^{\text{non-sec}}(t) + S_{-1}^{\text{non-sec}}(t).$$

(28)

By including incomplete excitation and the intermolecular dipolar interactions, one arrives at the final model

$$K_{\text{LaserIMD}}^{\text{non-sec}}(t,r) = B(t)(\lambda S_{\text{LaserIMD}}^{\text{non-sec}}(t,r) + 1 - \lambda).$$

(29)

Unlike it was the case for the secular approximation, the integrals are difficult to solve analytically and further insight in ~~these~~ this expression will be gained by numerical integrations in the next sections. However, it can already be seen without further calculations that with the non-secular terms the ZFS has an influence in LaserIMD and that the resulting kernel no longer corresponds to the kernel $K_{\text{DEER}}(t,r)$ of the $S = 1/2$ case.

2.3 LiDEER

In LiDEER, the transient triplet label is observed and the permanent spin label is pumped. For simplicity, we will derive the expressions within the secular approximation first and afterwards turn to the case that includes the non-secular terms. Due to the limited excitation bandwidth of the observer pulse, either the transition between the states with $m_T = 1$ and $m_T = 0$ or the states with $m_T = 0$ and $m_T = -1$ of the transient triplet label is excited. If the transition between the states $m_T = 1$ and $m_T = 0$ is excited, the excited coherence of the triplet spin will either evolve with the frequency $\omega_{+\frac{1}{2},\,1\leftrightarrow0}^{\text{sec}} = E_{+\frac{1}{2},\,+1}^{\text{sec}} - E_{+\frac{1}{2},\,0}^{\text{sec}}$ or $\omega_{-\frac{1}{2},\,1\leftrightarrow0}^{\text{sec}} = E_{-\frac{1}{2},\,+1}^{\text{sec}} - E_{-\frac{1}{2},\,0}^{\text{sec}}$, depending on whether the permanent spin label is in the state with $m_D = 1/2$ or $m_D = -1/2$. Pumping the permanent spin label at the time t will result in a transition from $m_D = +\frac{1}{2}$ to $m_D = -\frac{1}{2}$ -or vice versa- and the frequency $\omega_{+\frac{1}{2},\,1\leftrightarrow0}^{\text{sec}}$ or $\omega_{-\frac{1}{2},\,1\leftrightarrow0}^{\text{sec}}$ with which the coherence evolves will change accordingly. At the time of the echo, the coherence will have gained a phase $\phi = \omega_{\pm\frac{1}{2}\to\mp\frac{1}{2},\,+1\leftrightarrow0}^{\text{sec}} t$, where $\omega_{\pm\frac{1}{2}\to\mp\frac{1}{2},\,+1\leftrightarrow0}^{\text{sec}}$ are the LiDEER frequencies of the two coherence transfer pathways:

$$\omega_{+\frac{1}{2}\to-\frac{1}{2},\,+1\leftrightarrow0}^{\text{sec}} = \left(E_{+\frac{1}{2},+1}^{\text{sec}} - E_{+\frac{1}{2},\,0}^{\text{sec}} \right) - \left(E_{-\frac{1}{2},+1}^{\text{sec}} - E_{-\frac{1}{2},\,0}^{\text{sec}} \right) = \left(3\cos(\beta_{\text{dip}})^2 - 1 \right)\omega_{\text{dip}},$$

(30)

$$\omega^{\text{sec}}_{-\frac{1}{2}\to+\frac{1}{2},\,+1\leftrightarrow 0} = \left(E^{\text{sec}}_{-\frac{1}{2},\,+1} - E^{\text{sec}}_{-\frac{1}{2},\,0}\right) - \left(E^{\text{sec}}_{+\frac{1}{2},\,0} - E^{\text{sec}}_{+\frac{1}{2},\,-1}\right) = -\left(3\cos(\beta_{\text{dip}})^2 - 1\right)\omega_{\text{dip}}. \tag{31}$$

When the other transition of the triplet spin from $m_\text{T} = 0$ and $m_\text{T} = -1$ is excited by the observer pulse, the frequencies are the same:

$$\omega^{\text{sec}}_{+\frac{1}{2}\to-\frac{1}{2},\,0\leftrightarrow -1} = \left(E^{\text{sec}}_{+\frac{1}{2},\,+1} - E^{\text{sec}}_{+\frac{1}{2},\,0}\right) - \left(E^{\text{sec}}_{-\frac{1}{2},\,+1} - E^{\text{sec}}_{-\frac{1}{2},\,0}\right) = \left(3\cos(\beta_{\text{dip}})^2 - 1\right)\omega_{\text{dip}}, \tag{32}$$

$$\omega^{\text{sec}}_{-\frac{1}{2}\to+\frac{1}{2},\,0\leftrightarrow -1} = \left(E^{\text{sec}}_{-\frac{1}{2},\,+1} - E^{\text{sec}}_{-\frac{1}{2},\,0}\right) - \left(E^{\text{sec}}_{+\frac{1}{2},\,0} - E^{\text{sec}}_{+\frac{1}{2},\,-1}\right) = -\left(3\cos(\beta_{\text{dip}})^2 - 1\right)\omega_{\text{dip}}. \tag{33}$$

As those are the same frequencies as the ones in DEER with two $S = 1/2$ spins, one eventually arrives at the same kernel $K_{\text{DEER}}(t, r)$. This means that like it was the case in LaserIMD the secular terms of the ZFS cancel each other out, and there is no effect of the ZFS on the LiDEER trace. In contrast to LaserIMD in secular approximation, there are also no coherence transfer pathways with $\Delta m_\text{D} = 0$, so that the maximum achievable modulation depth in LiDEER is 100 %.

It seems obvious that the same non-secular terms that lead to change in the LaserIMD frequencies are also relevant in LiDEER. Therefore, the LiDEER frequencies were also determined from the energy levels $E^{\text{non}-\text{sec}}_{m_\text{D}, m_\text{T}}$ that include the effects of the ZFS:

$$\omega^{\text{non}-\text{sec}}_{+\frac{1}{2}\to-\frac{1}{2},\,+1\leftrightarrow 0} = \left(E^{\text{non}-\text{sec}}_{+\frac{1}{2},\,+1} - E^{\text{non}-\text{sec}}_{+\frac{1}{2},\,0}\right) - \left(E^{\text{non}-\text{sec}}_{-\frac{1}{2},\,+1} - E^{\text{non}-\text{sec}}_{-\frac{1}{2},\,0}\right)$$
$$= \left(\left(3\cos(\beta_{\text{dip}})^2 - 1\right) + 3\delta_{\text{ZFS}}\sin(2\beta_{\text{dip}})\right)\omega_{\text{dip}}, \tag{34}$$

$$\omega^{\text{non}-\text{sec}}_{-\frac{1}{2}\to+\frac{1}{2},\,+1\leftrightarrow 0} = \left(E^{\text{non}-\text{sec}}_{-\frac{1}{2},\,+1} - E^{\text{non}-\text{sec}}_{-\frac{1}{2},\,0}\right) - \left(E^{\text{non}-\text{sec}}_{+\frac{1}{2},\,0} - E^{\text{non}-\text{sec}}_{+\frac{1}{2},\,-1}\right)$$
$$= -\left(\left(3\cos(\beta_{\text{dip}})^2 - 1\right) + 3\delta_{\text{ZFS}}\sin(2\beta_{\text{dip}})\right)\omega_{\text{dip}}, \tag{35}$$

$$\omega^{\text{non}-\text{sec}}_{+\frac{1}{2}\to-\frac{1}{2},\,0\leftrightarrow -1} = \left(E^{\text{non}-\text{sec}}_{+\frac{1}{2},\,+1} - E^{\text{non}-\text{sec}}_{+\frac{1}{2},\,0}\right) - \left(E^{\text{non}-\text{sec}}_{-\frac{1}{2},\,+1} - E^{\text{non}-\text{sec}}_{-\frac{1}{2},\,0}\right)$$
$$= \left(\left(3\cos(\beta_{\text{dip}})^2 - 1\right) - 3\delta_{\text{ZFS}}\sin(2\beta_{\text{dip}})\right)\omega_{\text{dip}}, \tag{36}$$

$$\omega^{\text{non}-\text{sec}}_{-\frac{1}{2}\to+\frac{1}{2},\,0\leftrightarrow -1} = \left(E^{\text{non}-\text{sec}}_{-\frac{1}{2},\,+1} - E^{\text{non}-\text{sec}}_{-\frac{1}{2},\,0}\right) - \left(E^{\text{non}-\text{sec}}_{+\frac{1}{2},\,0} - E^{\text{non}-\text{sec}}_{+\frac{1}{2},\,-1}\right)$$
$$= -\left(\left(3\cos(\beta_{\text{dip}})^2 - 1\right) - 3\delta_{\text{ZFS}}\sin(2\beta_{\text{dip}})\right)\omega_{\text{dip}}. \tag{37}$$

It can be seen again that the ZFS leads to a shift in the dipolar frequencies. This shift is, besides the factor of 3, identical to the one that was obtained for the LaserIMD frequencies $\omega^{\text{non}-\text{sec}}_{+1}$ and $\omega^{\text{non}-\text{sec}}_{-1}$. From here, the next step is again the averaging over the orientations of the transient triplet label and the dipolar coupling vector that contribute to the LiDEER signal. However, this is even more complicated than it was in LaserIMD where all orientations are evenly excited by the laser-flash.

12

In LiDEER the triplet spins are also excited by microwave pulses ~~who~~ which typically have a bandwidth that is much more narrow than the EPR spectrum of the transient triplet label. For example, the frequently used porphyrin labels have an EPR spectrum that is over 2 GHz broad (Di Valentin et al., 2014) of which a typical rectangular microwave pulse with a length of 10 ns can only excite roughly 120 MHz (Schweiger and Jeschke, 2001). Therefore, not all orientations of the transient triplet
5 labels contribute to the LiDEER signal and it is rather tedious to even derive an expression for the integrals that describe the orientation averaging. To circumvent this problem, the LiDEER traces will be calculated by time-domain simulations with weak microwave pulses in the next sections.

3 Materials and methods

3.1 Simulations

10 The powder averages for LaserIMD were performed by a numerical integration of Eq. (25) -(27) with home-written MATLAB (version 2020b) scripts. For the angle β_{dip} a linear, equidistant grid from 0 to $\frac{\pi}{2}$ was used. Each value was weighted proportional to $\sin(\beta_{\mathrm{dip}})$. For the orientation of the transient triplet label, a grid with all three Euler ang~~el~~les α_{T}, β_{T} and γ_{T}, including the corresponding weights, was calculated according to the REPULSION approach (Bak and Nielsen, 1997; Hogben et al., 2011) with the software package *Spinach* version 2.6.5625 (Hogben et al., 2011). To check for a sufficient convergence,
15 a test run with an increasing numbers of points for the two grids was simulated. The test run was stopped when the relative change $\Delta\epsilon$ in the simulated signal, when the number of grids points was increased, was below 1 %. For β_{dip} a grid size of 200 points was sufficient, whereas for α_{T}, β_{T} and γ_{T} 12800 points were necessary. For details of the convergence behavior, see S3.

The time-domain simulations for LiDEER were performed with *Spinach* version 2.6.5625 (Hogben et al., 2011). The powder
20 averaging was done with the same grids that were used for LaserIMD. For details see S7̶8. The source code for the LiDEER simulations can be downloaded at https://github.com/andreas-scherer/LiDEER_simulations.git

3.2 Experiments and data analysis

LaserIMD and LiDEER measurements were performed on the two peptides TPP-pAA$_5$-NO• and TPP-pAA$_{10}$-NO• shown in Figure 3~~Fig. 3~~. They were purchased from Biosynthan (Berlin) as powder samples and used without further purification. They
25 were dissolved in MeOD/D$_2$O (98/2 vol.%) and prior to freezing in liquid nitrogen, they were degassed with three freeze-pump-thaw cycles. Light excitation was performed at a wavelength of 510 nm by an Nd:YAG laser system from Ekspla (Vilnius) that was coupled into the resonator via a laser fiber. EPR measurements were performed on a commercial Bruker E580 spectrometer, X-band measurements in an ER4118X-MS3 resonator and Q-band measurements in an ER5106QT-2 resonator. In X-band the resonator was critically coupled to a Q-value of ≈ 900-2000 ~~for higher sensitivity~~ and in Q-band it

13

was overcoupled to a Q-value of ≈ 200. LaserIMD was recorded with the pulse sequence $\pi/2 - \tau - \pi - t$ - laser pulse - $(\tau\text{-}t)$ - echo (Hintze et al., 2016). A 2-step phase cycle was implemented for baseline correction. Signal averaging was done by recording 10 shots per point. The zero-time correction was performed by recording a short reLaserIMD (Dal Farra et al., 2019a) trace as reported in (Scherer et al., 2022). LiDEER measurements were performed with the pulse sequence: laser pulse – DAF

5 $- \pi/2 - \tau_1 - \pi - t - \pi_{\text{pump}} \;\;\text{pump}\;\; (\tau_1 + \tau_2 - t) - \pi - \tau_2 - \text{echo}$ (Di Valentin et al., 2014). The delay-after-flash (DAF) was set to 500 ns and τ_1 to 400 ns. Nuclear modulation averaging was performed by varying the τ_1 time in 8 steps with $\Delta\tau_1 = 16$ ns. Phase cycling was performed with an 8-step scheme ((x) [x] xp x) as proposed by (Tait and Stoll, 2016). The LiDEER data were analysed with the python software package *DeerLab* (version 0.13.2) (Fábregas Ibáñez et al., 2020) and *Python* 3.9 with the DEER kernel $K_{\text{DEER}}(t, r)$ and Tikhonov regularization. A 3D homogenous background function was used and the

10 regularization parameter was chosen according to the Akaiki information criterion (Edwards and Stoll, 2018). The validation was performed with bootstrapping by analyzing 1000 samples that are generated with artificial noise. The error was then calculated as the 95% confidence interval. Further details can be found in S7 and S10.
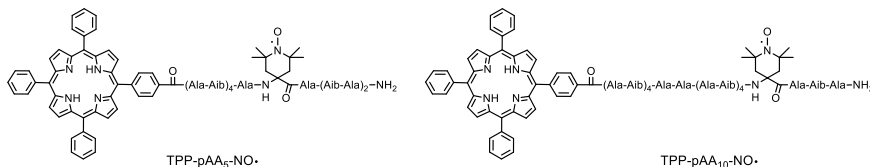
Figure 3: Chemical structures of the peptides TPP-pAA$_5$-NO• and TPP-pAA$_{10}$-NO• with the letter code Ala: L-alanine and Aib: α-isobutyric
15 acid.

4 Results and Discussion

4.1 LaserIMD simulations

An initial simulation to study the effect of the ZFS in LaserIMD was performed for X-band ($v\nu_{\text{T}} = 9.3$ GHz) with a dipolar coupling that corresponds to a distance of $r = 2.2$ nm, a ZFS of $D = 1159$ MHz and $E = -238$ MHz and zero-field

20 populations $P_{\text{x}} = 0.33$, $P_{\text{Y}} = 0.41$ and $P_{\text{Z}} = 0.26$. The ZFS and zero-field populations correspond to TPP the porphyrin derivative TPP that is often used to perform LaserIMD and LiDEER measurements (Di Valentin et al., 2014; Hintze et al., 2016; Di Valentin et al., 2016; Bieber et al., 2018; Bertran et al., 2020). For simplicity, a complete excitation of the transient triplet label ($\gamma = 1$) was assumed and effects of the background were ignored no background was added ($B(t) = 1$). For a more detailed analysis, the contributions from the three coherence transfer pathways with $\Delta m_{\text{T}} = 1, 0, -1$, termed

25 $V_{+1}^{\text{non}-\text{sec}}(t)$, $V_0^{\text{non}-\text{sec}}(t)$ and $V_{-1}^{\text{non}-\text{sec}}(t)$, are simulated separately and presented in Figure 4 Fig. 4 together with their resulting sum $V_{\text{LaserIMD}}^{\text{non}-\text{sec}}(t)$. They are also compared with the corresponding traces from the secular approximation $V_{\text{LaserIMD}}^{\text{sec}}(t)$, $V_{+1}^{\text{sec}}(t)$, $V_0^{\text{sec}}(t)$ and $V_{-1}^{\text{sec}}(t)$, where the ZFS is ignored. The comparison of the traces including and excluding

14

the ZFS ($V_{+1}^{non-sec}(t)$ and $V_{-1}^{non-sec}(t)$ with $V_{+1}^{sec}(t)$ and $V_{-1}^{sec}(t)$) in <u>Figure 4</u>~~Fig. 4~~a and c shows that there is no visible effect of the ZFS in the traces $V_{+1}^{non-sec}(t)$ and $V_{-1}^{non-sec}(t)$ and they look virtually identical to $V_{+1}^{sec}(t)$ and $V_{-1}^{sec}(t)$. The frequency shift $\delta_{ZFS}\sin(2\beta_{dip})\omega_{dip}$ seems to be averaged out after integration for ~~this~~ these terms. The situation is different in the case of $V_0^{non-sec}(t)$ and $V_0^{sec}(t)$ in <u>Figure 4</u>~~Fig. 4~~b. Whereas $V_0^{sec}(t)$ is a constant function of time and does not contribute to the

5 echo modulation, $V_0^{non-sec}(t)$ shows a continuous decay of the echo intensity with increasing time. This decay does not contain any additional dipolar oscillations and its shape does not seem to follow any obvious simple mathematical law. For the full LaserIMD traces in <u>Figure 4</u>~~Fig. 4~~d, this means that, whereas without taking ZFS into account the trace $V_{LaserIMD}^{sec}(t)$ looks like a $S = 1/2$ DEER trace with and a modulation depth of $\lambda = 66.\overline{6}$ %. , the trace $V_{LaserIMD}^{non-sec}(t)$ with the ZFS shows the same dipolar oscillations but on top of a decay. This also means that, due to the coherence transfer pathway with $\Delta m_T = 0$

10 also resulting in a variation of the echo intensity, the modulation depth of LaserIMD is increased by the ZFS and values higher than $66.\overline{6}$ %. can be reached.

a) $V_{+1}^{non-sec}(t)$

b) $V_0^{non-sec}(t)$

c) $V_{-1}^{non-sec}(t)$

d) $V_{LaserIMD}^{non-sec}(t)$

15
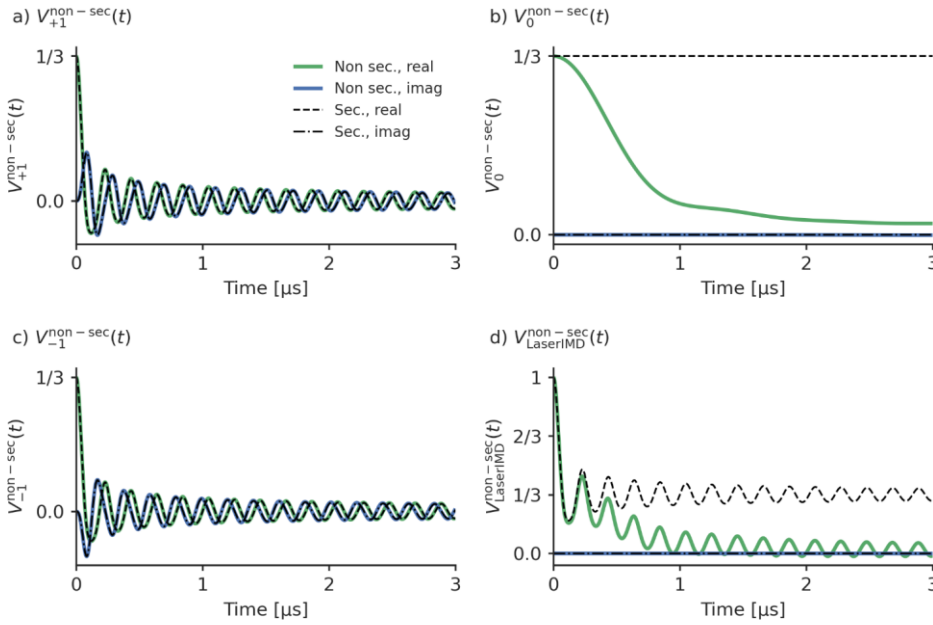
Figure 4: Comparison of simulated LaserIMD traces with and without non-secular interactions with the values $D = 1159$ MHz, E= -238 MHz and $P_x = 0.33$, $P_y = 0.41$ and $P_z = 0.26$, ~~ω_T~~$\nu_T = 9.3$ GHz (X-band) and $r = 2.2$ nm. a) $V_{+1}^{non-sec}(t)$, b) $V_0^{non-sec}(t)$, c) $V_{-1}^{non-sec}(t)$, d) $V_{LaserIMD}^{non-sec}(t) = V_{+1}^{non-sec}(t) + V_0^{non-sec}(t) + V_{-1}^{non-sec}(t)$.

The frequency shift caused by the non-secular terms of the ZFS in LaserIMD depends not only on D and E, but also on the zero-field populations P_x, P_y and P_z, the Zeeman frequency ~~$\nu\omega_T$~~ and the distance r (see Eq. (21) -(24)). The influence of these parameters was studied by simulating additional LaserIMD traces with different ~~ZFSs, zero-field populations,~~ magnetic field strengths, ZFS values, zero-field populations, and distance~~s~~ distributions (see Figure 5~~Fig. 5~~ and Figure 6). In Figure 5~~Fig. 5~~a, two LaserIMD traces in X- and Q-band ($\nu\omega_T = 9.3$ GHz and ~~ω_T~~$\nu_T = 34.0$ GHz) with TPP as a transient triplet label and a distance of $r = 2.2$ nm are compared. Figure 5~~Fig. 5~~b shows the comparison between the ZFS of TPP ($D = 1159$ MHz and E= -238 MHz) and a stronger ZFS of $D = 3500$ MHz and E= -800 MHz, as such high values are possible for some labels like Rose Bengal and Erythrosin B (Williams et al., 2020; Bertran et al., 2022b). Both simulations were performed in Q-band with $r = 2.2$ nm. Figure 5c shows three simulations with the population of the zero-field triplet states being completely assigned to either P_x, P_y or P_z. In Figure 5~~Fig. 5~~de, the effect of different distances of $r = 2.2$ nm and $r = 5$ nm on $V_0^{non-sec}(t)$ is shown for TPP in Q-band. ~~Fig. 5d shows three simulations with the population of the zero-field triplet states spin being completely assigned to either P_x, P_y or P_z.~~ The simulations in Figure 5 were all done with a single distance. To study the influence of the width of the distance distribution on $V_0^{non-sec}(t)$, additional simulations were performed with a Gaussian distance distribution with a mean of 3 nm and different standard deviations σ ranging from 0.05 nm to 3 nm. The results of these simulations are shown in Figure 6a (X-band) and Figure 6b (Q-band).

Figure 5~~Figure 5~~a, Figure 5~~Fig. 5~~b and Figure 5~~Fig. 5~~d~~c~~ show that there are no visible differences in the dipolar oscillations in $V_{+1}^{non-sec}(t)$ and $V_{-1}^{non-sec}(t)$, when the Zeeman frequency, ZFS or zero-field populations are changed. This can also be seen in the SI in S4, S5 and S6 where the traces for different Zeeman frequencies, ZFSs and distances are compared in more detail. This ~~fits to~~agrees with the former results in Figure 4~~Fig. 4~~ that the frequency shift due to the ZFS is virtually averaged out in a powder sample for $V_{+1}^{non-sec}(t)$ and $V_{-1}^{non-sec}(t)$, so changing the involved parameters should also have little effect. The situation is different for $V_0^{non-sec}(t)$, which, as it is shown in Figure 4~~Fig. 4~~c, ~~feels a stronger effect~~is more strongly affected by of the ZFS. The previously mentioned decay is faster for ~~a~~ lower Zeeman frequencies (see Figure 5~~Fig. 5~~a) and a stronger ZFS (see Figure 5~~Fig. 5~~b). Because δ_{ZFS} ultimately depends on the ratio of the ZFS to the Zeeman frequency, a higher ZFS and a lower Zeeman frequency both increase the magnitude of the frequency shift of $\omega_0^{non-sec}$ in the same way which leads to the same effect on the LaserIMD trace. ~~Fig. 5c shows that shorter distances also lead to a faster decay of $V_0^{non-sec}(t)$. As can be seen in Eq. (21) -(23), changing the distances from 2.2 to 5 nm leads to a rescale of the LaserIMD frequencies $\omega_{+1}^{non-sec}$, $\omega_0^{non-sec}$ and $\omega_{-1}^{non-sec}$ with r^{-3}. This distance dependency of the dipolar oscillations (not shown in Fig. 5c) is used in PDS for the calculation of the distance distributions. In the case of LaserIMD, the steepness of the decay of $V_0^{non-sec}(t)$ is an additional feature that depends on the distance between the spin labels.~~ The parameters that have the least influence on the LaserIMD trace are the zero-field populations (see Figure 5~~Fig. 5~~d~~c~~). Changing the populations of the zero-field states does not seem to affect the dipolar oscillations, as it was the case for different ZFSs and magnetic field strengths. This time, also

16

the decay of $V_0^{non-sec}(t)$ is barely affected by different zero-field populations. Figure 5d shows that shorter distances lead to a faster decay of $V_0^{non-sec}(t)$. As can be seen in Eq. (21) -(23), changing the distance r from 2.2 to 5 nm leads to an increase of the LaserIMD frequencies $\omega_{+1}^{non-sec}$, $\omega_0^{non-sec}$ and $\omega_{-1}^{non-sec}$ that scales with r^{-3}. This distance dependence of the dipolar oscillations (not shown in Figure 5c) is used in PDS for the calculation of the distance distributions. In the case of LaserIMD, the steepness of the decay of $V_0^{non-sec}(t)$ is an additional feature that depends on the distance between the spin labels. As can be seen in Figure 6 the width of the distance distribution also has an influence on the decay of $V_0^{non-sec}(t)$. In X-band (see Figure 6a) and for small standard deviations of $\sigma = 0.05$ nm, $V_0^{non-sec}(t)$ has a sigmoid like shape. Increasing the width has a twofold effect on the decay of $V_0^{non-sec}(t)$. Whereas the initial decay is steeper, on a long scale, the decay of $V_0^{non-sec}(t)$ is decreased for broader distance distributions. This can clearly be seen in the case of $\sigma = 3$ nm where for $t < 1\ \mu$s $V_0^{non-sec}(t)$ decays faster for the simulation with $\sigma = 3$ nm than with $\sigma = 0.05$ nm, but for $t > 1\ \mu$s $V_0^{non-sec}(t)$ decays slower for $\sigma = 3$ nm than for $\sigma = 0.05$ nm. In Q-band where the decay of $V_0^{non-sec}(t)$ is generally slower, the simulations in Figure 6b show that here only the first effect is of relevance. It can be seen that the first part of the decay of $V_0^{non-sec}(t)$ is again steeper for broader distance distributions, but the second part where this behavior is inverted lies outside the time window. This means that in Q-band the width of the distance distribution has a smaller influence on the decay of $V_0^{non-sec}(t)$ than in Q-band.

Taken together, variation in the ZFS parameter, the population of the ZFS states and the employed magnetic field (X- or Q-band) do not affect the dipolar oscillations in $V_{+1}^{non-sec}(t)$ and $V_{-1}^{non-sec}(t)$. They mostly have an effect on the decay of $V_0^{non-sec}(t)$, such that a stronger larger ZFS parameters and lower magnetic fields will lead to a stronger additional decay in the LaserIMD trace. The additional decay is also stronger for shorter distances between the also depends on the distance distribution between the spin labels, it is faster for shorter distances and the shape of the decay also depends on the width of the distance distribution (in X-band more than in Q-band). and The decay of $V_0^{non-sec}(t)$ can therefore be used as an additional source of information for the calculation of the distance distribution.

a)

Q-band ($\nu_T = 34.0$ GHz)
X-band ($\nu_T = 9.3$ GHz)

$V_{LaserIMD}^{non-sec}(t)$

Time [μs]

b)

$D = 1159$ MHz
$E = -238$ MHz
$D = 3500$ MHz
$E = -800$ MHz

$V_{LaserIMD}^{non-sec}(t)$

Time [μs]

c)

$r = 5$ nm
$r = 2.2$ nm

$V_0^{non-sec}(t)$

Time [μs]

d)

$P_x = 1$
$P_y = 1$
$P_z = 1$

$V_{LaserIMD}^{non-sec}(t)$

Time [μs]
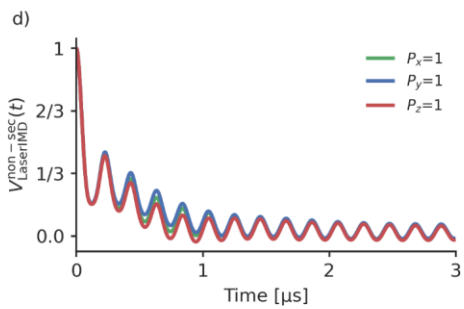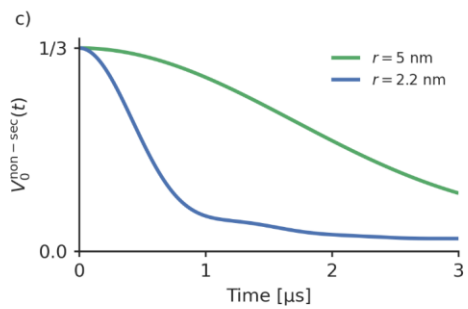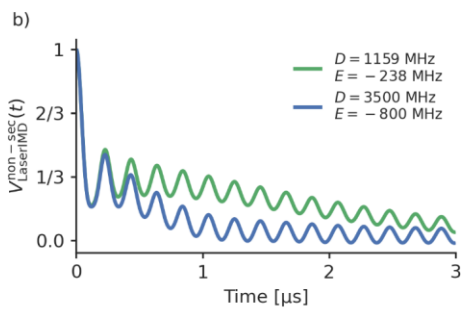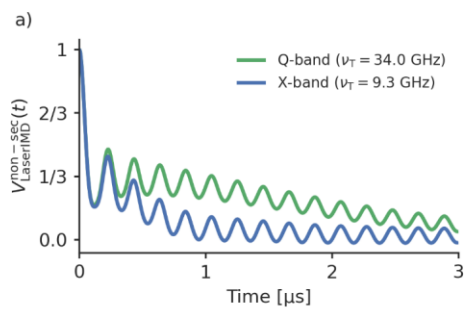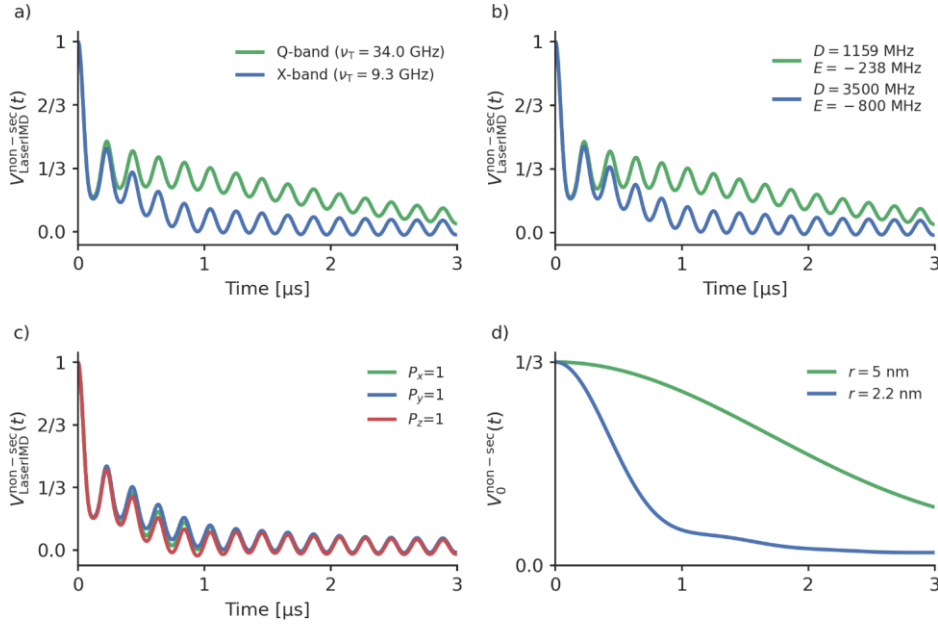
Figure 5: A comparison of different LaserIMD traces $V_{\text{LaserIMD}}^{\text{non-sec}}(t)$ with different parameters. The following values were used for the simulations. a) TNPP, $r = 2.2$ nm and $\omega\nu_T = 34$ GHz (green) and $\nu\omega_T = 9.3$ GHz (blue) b) $P_x = 0.33$, $P_y = 0.41$, $P_z = 0.26$, $r = 2.2$ nm, $\omega_T = 9.3$ GHz and $D = 1159$ MHz, $E = -238$ MHz (green) and $D = 3500$ MHz, $E = -800$ MHz (blue) c) TPP, $\nu\omega_T = 34$ GHz and $r = 2.2$ nm green) and $r = 5$ nm (blue) d) $D = 1159$ MHz, $E = -238$ MHz $r = 2.2$ nm, $\omega_T\nu_T = 9.3$ GHz and $P_x = 1$, $P_y = 0$, $P_z = 0$ (green), $P_x = 0$, $P_y = 1$, $P_z = 0$ (blue) and $P_x = 0$, $P_y = 0$, $P_z = 1$ (red).

Formatiert: Schriftart: Nicht Fett

19
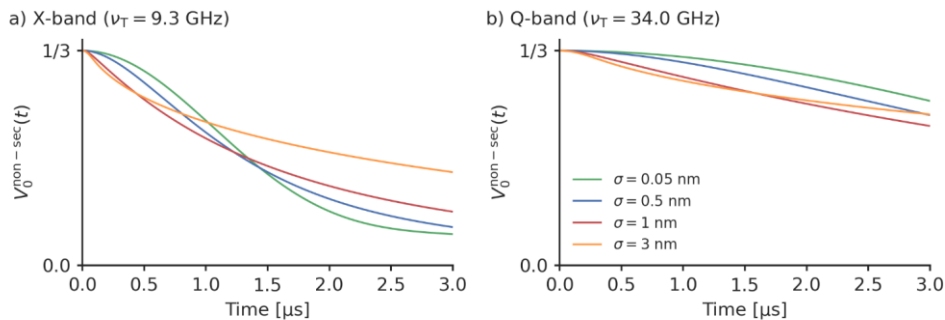
Figure 6; The influence of the width of the distance distribution on the decay of $V_0^{non-sec}(t)$ for TPP in a) X-band and b) Q-band. The simulations were performed for a Gaussian distance distribution width a mean of 3 nm and different standard deviations σ.

So far, all simulations only showed a visible effect of the ZFS on $V_0^{non-sec}(t)$, no significant influence on $V_{+1}^{non-sec}(t)$ and $V_{-1}^{non-sec}(t)$ was observed. To check if and when the ZFS has also an influence on $V_{+1}^{non-sec}(t)$ and $V_{-1}^{non-sec}(t)$, we performed additional simulations where the effect of the ZFS is expected to be stronger. This can be obtained by either lower Zeeman frequencies or higher ZFS values. As the effect on δ_{ZFS} is the same in both cases, the ratio of D and the Zeeman frequency of the triplet ν_T can be defined as:

$$q = \frac{D}{2\pi\nu_T} \tag{38}$$

For simplification, the ZFS was assumed to be axial with $E = 0$. This simplifies the expression of δ_{ZFS} to:

$$\delta_{ZFS} = \frac{3}{4}q \sin(2\beta_T)\cos(\alpha_T) \tag{39}$$

The simulation in X-band with TPP from Figure 4 corresponds to a ratio where q is approximately 0.13. Here, we tried values for q of up to 1. Figure 7 shows the sum of $V_{+1}^{non-sec}(t)$ and $V_{-1}^{non-sec}(t)$ of these simulations and compares it to a trace where the effect of the ZFS has been ignored. It can be seen that up to $q = 0.5$, the traces are negligibly affected by the ZFS. For higher values, the dipolar oscillations start to get shifted to slightly higher frequencies and are also smoothed out more quickly. Analyzed with the over-simplified kernel $K_{DEER}(t, r)$ of the $S = 1/2$ model, this would result in a shift to smaller distances and an artificial broadening of the distance distribution. However, for experimentally relevant distance distributions with a finite width, the oscillations typically fade out much quicker and cases where four oscillations can be resolved are scarce. In such a case, the observed influence of the ZFS for high values of q can be expected to almost negligible. Furthermore, as $q = 1$ is equivalent to a ZFS that is in the same order of magnitude as the Zeeman frequency, this is not relevant for most practical applications, as LaserIMD is typically performed at X- or Q-band ($\nu_T = 9.3$ GHz or $\nu_T = 34.0$ GHz) and all transient triplet labels used so far have a ZFS value D below 4 GHz (Dal Farra et al., 2019b; Williams et al.,

20

2020). Even in the most extreme case, this would result in values for q smaller than 0.5. Consequently, th~~ise~~ effect of the ZFS on $V_{+1}^{\text{non}-\text{sec}}(t)$ and $V_{-1}^{\text{non}-\text{sec}}(t)$ is not relevant for most experiments and even though the ~~contributions from~~ $V_{+1}^{\text{non}-\text{sec}}(t)$ and $V_{-1}^{\text{non}-\text{sec}}(t)$ can in principle b~~e~~y influenced by the ZFS, it seems to be a safe assumption that the ZFS in LaserIMD affects only the decay in $V_0^{\text{non}-\text{sec}}(t)$ and not the dipolar oscillations in $V_{+1}^{\text{non}-\text{sec}}(t)$ and $V_{-1}^{\text{non}-\text{sec}}(t)$.
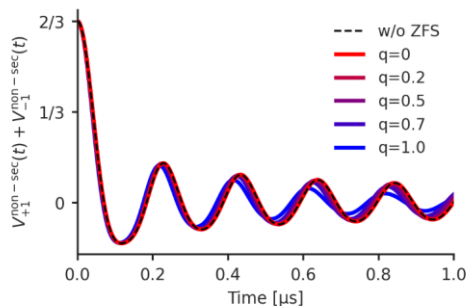
Figure 76: a) The sum of $V_{+1}^{\text{non}-\text{sec}}(t)$ and $V_{-1}^{\text{non}-\text{sec}}(t)$ for different values of q and $P_x = 0.33$, $P_y = 0.41$, $P_z = 0.26$ and $r = 2.2$ nm. Only the real part is shown.

As was stated before, in the secular approximation, LaserIMD traces can be analysed with the kernel $K_{\text{DEER}}(t,r)$ of the $S = 1/2$ model. To check to what exten~~td~~ this is true when the ZFS is not negligible, we simulated LaserIMD traces that were subsequently analyzed with $K_{\text{DEER}}(t,r)$. To mimic experimental condition~~s~~ more closely, we assumed an incomplete excitation of the transient triplet label and the intermolecular dipolar background was also considered. TPP was used as transient triplet label with a distance to the permanent spin label of $r = 2.2$ nm and a modulation depth of $\lambda = 50$ %, which roughly correspond to the values that can be typically achieved in experiments. Simulations were performed in X- and Q-band with different background decay rates varying between $k = 0.0$ μs^{-1} (no background) to $k = 0.4$ μs^{-1}. The resulting traces were then analyzed with $K_{\text{DEER}}(t,r)$ and Tikhonov regularization (see details in S7).
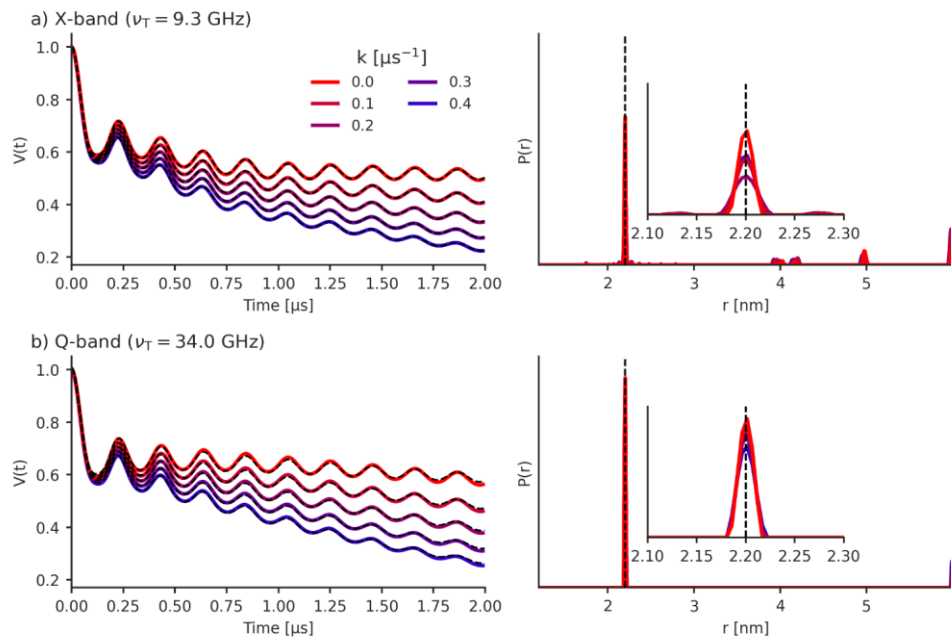
Figure 8~7~: Simulation~ed~s LaserIMD traces $V_{\text{LaserIMD}}^{\text{non-sec}}(t)$ including ~the non-secular terms~the ZFS for TPP as transient triplet label and $r = 2.2$ nm in a) X-band (~$\nu\omega_T$~ = 9.3 GHz) and b) Q-band (~$\omega\nu_T$~ = 34.0 GHz). The background decay that was used for the simulation was varied between $k = 0.0 \ \mu s^{-1}$ and $k = 0.4 \ \mu s^{-1}$. The left side shows the simulated traces (with the fits as dashed black line) and the right side shows the distance distributions that were obtained with Tikhonov regularization with $K_{\text{DEER}}(t, r)$. The true distance of $r = 2.2$ nm is plotted as dashed black line.

22

Table 1: The background decay values and modulation depths that were determined for the simulations from Figure 8~~Fig. 7~~. The modulation depth for the simulations was always set to $\lambda = 50$ %.

k [µs^{-1}]	X-band ($\nu_T = 9.3$ GHz)		Q-band ($\nu_T = 34.0$ GHz)	
	k_{fit} [µs^{-1}]	λ_{fit} [%]	k_{fit} [µs^{-1}]	λ_{fit} [%]
0.0	0.00	47	0.07	32
0.1	0.00	54	0.17	32
0.2	0.00	61	0.26	33
0.3	0.00	66	0.35	34
0.4	0.01	70	0.44	36

The simulations and fitted distance distributions can be seen in Figure 8~~Fig. 7~~ and the background decay rates and modulations depths that were obtained by the fits in Table 1. Figure 8~~Figure 7~~ shows that the fits agree well with the simulated data and the main peak of the distance distribution at $r = 2.2$ nm is fitted appropriately in X- as well as in Q-band. However, there can be additional artiefact peaks in the distance distributions, and the fitted modulation depths and background decay rates can be erroneous (see Table 1). This is particularly pronounced in X-band, which shows artiefacts in the distance distribution between 3.9 nm and 5 nm and at the higher distance end. Moreover, the background decay rates and modulation depths deviate significantly from the values that were originally used for the simulations. The simulations in X-band are always fitted with a background decay rate close to zero ($k_{\text{fit}} \approx 0.0\ \mu s^{-1}$), even in the cases where the strongest background was included ($k = 0.4\ \mu s^{-1}$) in the simulation. The modulation depth was fitted with values from 47 % to 70 % and varies significantly for different background decays. In Q-band, the fitted parameters ~~correspond~~ are closer to the input values of the simulations. The distance artiefacts that appeared in X-band between 3.9 nm and 5 nm have disappeared, and only those at the long distance limit remain. In Q-band the fitted background decay is always a bit larger than the true value. Except for the case were the true background decay is set to $k = 0\ \mu s^{-1}$, the deviation of the fitted and the true background decay is smaller in Q-band than in X-band.~~The obtained background decay rates correspond better with the true values, but are always larger as them~~. Only the obtained modulation depths are less accurate than in X-band and fitted to values between 32 % and 36 %. Even though, these simulations are only anecdotal evidence and generalizations from these data must be taken with caution, they show that when LaserIMD data are analyzed with $K_{\text{DEER}}(t,r)$ it is possible to extract the main distance peak correctly. Analyzing LaserIMD traces with $K_{\text{DEER}}(t,r)$ can thus be an option in situations where the ZFS values and zero-field populations of the transient triplet label are unknown and their effect cannot be included in the analysis. However, this way of analyzing LaserIMD data can give arteifacts at higher distances and also errors in the obtained modulation depth and background decay rate. This is particularly pronounced for low magnetic fields (e.g. X-band) and similar results can be expected for transient triplet labels with higher ZFS values.

4.2 LiDEER simulations

In LaserIMD, transient triplet labels of all orientations are excited by the laser flash and contribute to the signal, thus an integration over all ~~corresponding Euler angelles~~orientations ~~needs to be~~was performed (Eq. (25) -(27)) to calculate the LaserIMD signal. Contrary to that, in LiDEER the transient triplet labels are additionally excited by microwave observer pulses. As the spectrum of many transient triplet labels exceeds the excitation bandwidth of these pulses (Di Valentin et al., 2014; Williams et al., 2020; Krumkacheva et al., 2019), only a small number of orientations within the excitation bandwidth contribute to the signal. Because the frequency shift δ_{ZFS} of the LiDEER frequencies (Eq. (34) -(37)) depends on the orientation of the transient triplet labels, the choice of the observer frequency influences the shape of the LiDEER trace.

In experiments, when the commonly used nitroxides or other spin labels with $g_D \approx 2$ are used as pump spin, the resonator bandwidth allows to use only the $Y^\pm$ peaks as observer position, because the other parts of the EPR spectrum of the transient triplet label lie outside the resonator ~~profile~~bandwidth (Bieber et al., 2018; Bowen et al., 2021). Figure 9 shows the orientations of the triplet label TPP that in this case contribute to the LiDEER signal. The contribution of the orientations where the Y axis of eigenframe of the ZFS is parallel to the external magnetic field ($\beta_T = \pi/2$ and $\gamma_T = \pi/2$) is eponymous for the $Y^\pm$ peaks. For this orientation, the frequency shift $\delta_{ZFS} = 0$ and the ZFS has no effect on the LiDEER trace. However, it can be seen that other orientations are also excited if the observer pulses are placed on either of the $Y^\pm$ peaks. For these contributions it cannot guaranteed that δ_{ZFS} is always zero, so that there might still be an effect of the ZFS.
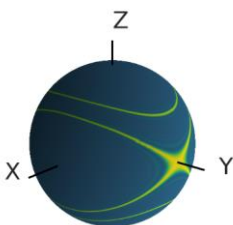
Figure 9: The orientations (shown in yellow) of the transient triplet label that are excited by a rectangular π pulse with a pulse length of 20 ns that is placed on the Y^+ peak of EPR spectrum of TPP in Q-band. For the calculation, the magnetic field was set to $B = 1.2097$ T and the pulse frequency was set to 33.646 GHz. The position of the pulse relative to the EPR spectrum is shown in Fig. S7. The angle β_T is the polar angle of the depicted sphere and the angle γ_T is the azimuthal angle.

~~As the LiDEER frequencies (Eq. (34) -(37)) depend on the orientation of the transient triplet label when the ZFS is included, the trace should change when the observer pulse excites different parts of the spectrum. For some orientations, the frequency shift due to the ZFS vanishes and the LiDEER frequencies are identical to the DEER frequencies. One example thereof are the canonical orientations X, Y and Z, because the Euler angles for these orientations are $\beta_T = \frac{\pi}{2}$ and $\gamma_T = 0$ for the X orientation,~~

24

$\beta_T = \frac{\pi}{2}$ and $\gamma_T = \frac{\pi}{2}$ for the Y orientation and $\beta_T = 0$ and $\gamma_T = 0$ for the Z orientation (Weil and Bolton, 2007) and according to Eq. (24), $\delta_{ZFS} = 0$ for these angles. In experiments, when the commonly used nitroxides or other spin labels with $g_D \approx 2$ are used as pump spin, the resonator bandwidth allows to use only the Y"-peaks as observer position, because the other parts of the spectrum lie outside the resonator profile (Bieber et al., 2018). Noteworthy, in the powder case, there are several orientations that contribute to the Y$^+$ peaks (Richert et al., 2017), not only the Y orientation, and an influence of the ZFS cannot be excluded for all of them. Therefore, to To study the effect of the ZFS in LiDEER, numerical time-domain simulations for different ZFS values in X- and Q-band were performed. The traces were then analyzed with $K_{DEER}(t,r)$ and Tikhonov regularization to check for artifacts in the thereby obtained distance distributions. The microwave pulses were placed on the Y$^+$ peak of the EPR spectrum and had a finite length, power and bandwidth so that only the parts of the spectrum around the Y$^+$ peak contribute to the signal orientations that are shown in Figure 9 contribute to the LiDEER signal, as it is the case in the experimental setup. A simulation for TPP as transient triplet label was performed in X- and Q-band and an additional simulation with a larger ZFS of $D = 3500$ MHz and $E = -800$ MHz was performed in X-band. The permanent spin label was included as a doublet spin with an isotropic g-value ($g_D = 2$) and without any additional hyperfine interactions. The distance was set to $r = 2.2$ nm and no background from intermolecular spins was included. To check for artifacts that occur in distance distributions if the ZFS is ignored in data analysis, the simulated LiDEER traces were analyzed with $K_{DEER}(t,r)$ and Tikhonov regularization. The details of the calculation of the distance distribution in S7 and the details of the simulations can be found in S8.
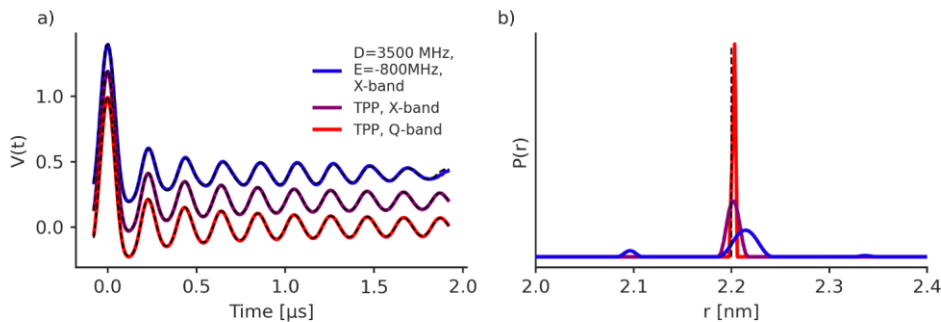
Figure 108: a) LiDEER simulations with the observer pulse placed on the Y$^+$-peak of the EPR spectrum of the transient triplet label in different frequency bands and with different ZFS. The traces are shifted by 0.2 for better visibility. For Q-band and TPP, the magnetic field was set to 1.2097 T and the observer frequency to 33.646 GHz; for X-band, the magnetic field was set to 0.33 T, which for TPP corresponds to an observer frequency of 9.042 GHz and for a ZFS with $D = 3500$ MHz and $E = -800$ MHz to an observer frequency of 9.042 GHz. The position of the observer and pump pulse with respect to the EPR spectrum is shown in Fig. S7a, c and e. The further parameters were $P_x = 0.33$, $P_y = 0.41$, $P_z = 0.26$ and $r = 2.2$ nm. The numerical simulations were fitted with Tikhonov regularization. The fits are shown as dashed black lines. b) The corresponding distance distribution. The true distance of $r = 2.2$ nm is plotted as dashed black line.

Figure 10Fig. 8a shows the simulated LiDEER traces and Figure 10Fig. 8b the obtained distance distributions. The differences in the LiDEER traces for different ZFS and Zeeman frequencies are smaller than they are in LaserIMD (see Figure 4Fig. 4). This is because in LiDEER, there is no equivalence for the coherence transfer pathway with $\Delta m_\text{T} = 0$ that showed the strongest dependency on the ZFS and magnetic fields in LaserIMD (see Figure 5Fig. 5). The distance distribution for TPP in Q-band

5   shows a narrow peak at 2.20 nm with a full width at half maximum (FWHM) of 0.004 nm. This fits to the 2.20 nm (FWHM = 0 nm) that were used for the simulation. In X-band, the distance distribution with TPP is also centered at 2.20 nm, but gets broadened to a FWHM of 0.014 nm. This trend increases for the large ZFS with $D = 3500$ MHz and $E = -800$ MHz in X-band. Here, the distance distribution gets even broader with an FWHM of 0.028 nm and is now also shifted to a center of $\approx$ 2.22 nm. This behavior fits to the results of LaserIMD in Figure 7Fig. 6, where the shifts of the dipolar oscillation get also

10   larger when the ZFS is large compared to the Zeeman frequency. However, it must also be stated that the observed shifts of the distance distribution are still rather small here and should be below the resolution limit that is relevant in most experiments. Additional traces, where the observer pulse is set off-resonance to the canonical peaks were also performed and are presented in S9. Here, especially for the case of $D = 3500$ MHz and $E = -800$ MHz in X-band, the dipolar trace show more significant differences from the case with excitation off the $Y^\pm$-peakeffect of the ZFS can clearly be seen and the LiDEER trace of the

15   simulation with $D = 3500$ MHz and $E = -800$ MHz in X-band shows strong deviations from the other traces that were simulated with a smaller ZFS. The dipolar oscillations fade out much faster, which also leads to a stronger broadening of the distance distributions. However, for experimentally relevant cases with distance distributions of a finite width, the oscillations in the dipolar trace fade out much faster anyway. It is to be expected that in these cases, the effect of the ZFS on the LiDEER trace are rather small and that therefore artifacts in the distance distribution are not so pronounced, even in the case when the

20   observer pulses are set to a non-canonical orientation. This means that in general the ZFS has an effect on LiDEER and the LiDEER trace changes, when different parts of the EPR -spectrum of the transient triplet label are used for excitation by the observer pulses. However, in the special case when either of the $Y^\pm$ peaks is used as position for the observer pulse, the effect of the ZFS can be suppressed and LiDEER traces can be analysedanalyzed with the $K_\text{DEER}(t, r)$ kernel without introducing significant artiefacts in the distance distribution. Thise is

25   particularly true valid for TPP -and other transient triplet labels with a similar ZFS- in Q-band.

4.3 Experiments

To experimentally confirm the theoretical finding that the ZFS has an influence on the shape of the LaserIMD trace, LaserIMD measurements were performed at different magnetic field strengths at X- and Q-band and with two model systems with a shorter and longer distances between the labels. This should result in scenarios were the ZFS has either a weak effect on the

30   trace (high magnetic field strength and long distance) or strong effect (low magnetic field strength and short distance). The LaserIMD experiments were simulated with the newly derived model that includes the ZFS. The distance distributions and background decay rates that were used for these simulations of the LaserIMD traces were determined with LiDEER. The

26

measurements were performed with the peptides TPP-pAA$_5$-NO• and TPP-pAA$_{10}$-NO•. They contain TPP as transient triplet label and the nitroxide TOAC as permanent spin label. Both labels are separated by a rather rigid helix consisting of L-alanine and α-isobutyric acid (Di Valentin et al., 2016).
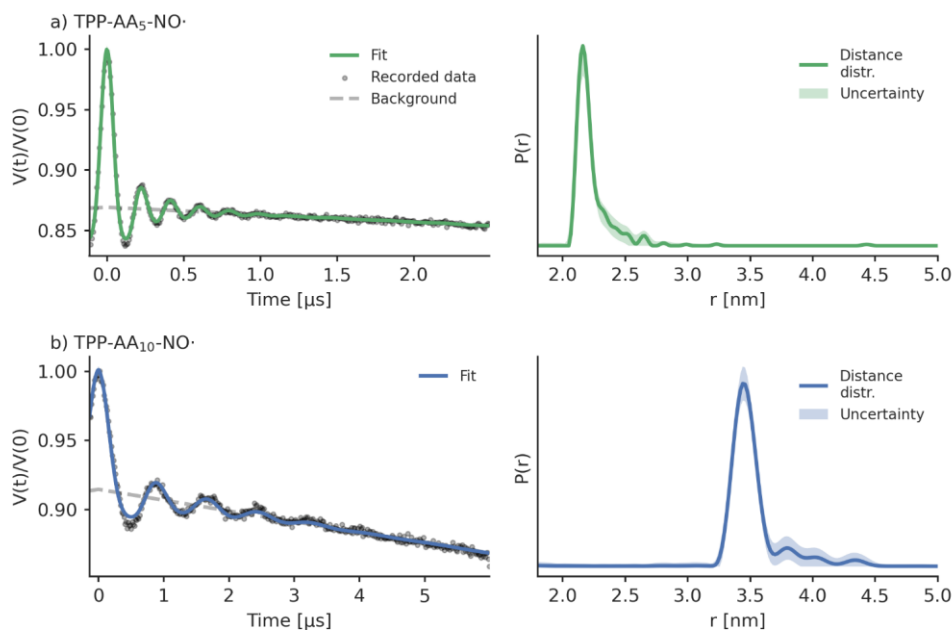
Figure 1~~1~~9: Experimental LiDEER data of the two peptides, all recorded in Q-band at 30 K in MeOD/D$_2$O (98/2 vol.%). a) TPP-pAA$_5$-NO• and b) TPP-pAA$_{10}$-NO•. The raw data are depicted on the left side as grey dots with the fits as straight line, the background fit is depicted as dashed grey line. The distance distributions obtained with Tikhonov regularization (Fábregas Ibáñez et al., 2020) is shown on the right side. The shaded areas correspond to the 95% confidence intervals that were obtained with bootstrapping.

So far, the LaserIMD simulations that were described above did mostly only invoke a single delta-like distance. To simulate LaserIMD for an entire distance distribution in a fast way, the dipolar kernel $K_{\text{LaserIMD}}^{\text{non−sec}}(t, r)$ needs to be calculated. Therefore, we implemented a C++ software tool that can perform the numerical integration of Eq. (25) -(27) to calculate $S_{\text{LaserIMD}}^{\text{non−sec}}(t, r)$. It allows the user to specify different ZFS values, zero-field populations and Zeeman frequencies. The background decay and modulation depth can then be included afterwards to obtain the full ~~k~~Kernel $K_{\text{LaserIMD}}^{\text{non−sec}}(t, r)$ (see Eq. (29)). The obtained kernel can for example be used in combination with the software DeerLab (Fábregas Ibáñez et al., 2020) to analyze experimental LaserIMD traces. The program including its source-code is available at github (https://github.com/andreas-

27

scherer/LaserIMD_kernel). Here, it was used to calculate the kernel that corresponds to the experimentally determined parameters for TPP of the peptides TPP-pAA$_5$-NO• and TPP-pAA$_{10}$-NO• (ZFS values: $D = 1159$ MHz and $E = -238$ MHz and zero-field populations: $P_x = 0.33$, $P_Y = 0.41$ and $P_Z = 0.26$ (Di Valentin et al., 2014)) at the Zeeman frequencies that correspond to the used magnetic field strengths ($\nu\omega_T = 9.28$ GHz, $\nu\omega_T = 9.31$ GHz in X-band and $\omega\nu_T = 34.00$ GHz in Q-

5   band, see also S910). The distance distributions of TPP-pAA$_5$-NO• and TPP-pAA$_{10}$-NO• that were used for the LaserIMD simulations were obtained by LiDEER measurements. LiDEER traces were recorded in Q-band with the observer pulse placed on the Y$^-$ peak and analyzed with $K_{DEER}(t,r)$ and Tikhonov regularization, as the simulations in section 4.2 showed that no artiefacts are to be expected in this case. More details on the experiments and distance calculations can be found in S7 and S10. The results of the LiDEER measurements are shown in Figure 11Fig. 9 and the extracted distance distributions exhibit a

10   narrow peak at 2.2 nm for TPP-pAA$_5$-NO• and at 3.5 nm for TPP-pAA$_{10}$-NO• as expected (Bieber et al., 2018; Di Valentin et al., 2016). As the LaserIMD and LiDEER measurements have different modulation depths, the modulation depth of LiDEER λ_{LiDEER} cannot be used for the simulation of the LaserIMD. This makes the modulation depth of the LaserIMD traces $\lambda_{LaserIMD}$ the only parameter that is missing for the simulations. Therefore, the simulated LaserIMD traces were fitted to the measured ones by rescaling the modulation depth. As the background decay rate depends linearly on the modulation depth (Hu and

15   Hartmann, 1974; Pannier et al., 2000), it must be rescaled together with the modulation depth. For LaserIMD, we assume that coherence transfer pathways with $\Delta m_T = 0$ does not contribute to the background, as its decay of the echo intensity is on a much longer timescale than the dipolar oscillations that constitute the main contribution of the intermolecular background. Therefore, we additionally reduce the rescaled background decay rate by a factor of 2/3:

$$K_{LaserIMD}^{non-sec}(t,r)_{\lambda_{LaserIMD}} = \exp\left(-\frac{2}{3}\frac{\lambda_{LaserIMD}}{\lambda_{LiDEER}}k_{LiDEER}t\right)\left(\lambda_{LaserIMD}S_{LaserIMD}^{non-sec}(t,r) + (1-\lambda_{LaserIMD})\right) \quad (40)$$

$$V_{LaserIMD}(t)_{\lambda_{LaserIMD}} = K_{LaserIMD}^{non-sec}(t,r)_{\lambda_{LaserIMD}}P_{LiDEER}(r) \quad (41)$$

The simulated LaserIMD trace $V_{LaserIMD}(t)_{\lambda_{LaserIMD}}$ was fitted to the experimental LaserIMD data by varying the modulation

20   depth $\lambda_{LaserIMD}$ so that the root-mean-square displacement of the simulated and experimental traces was minimized. Simulations without the effect of the ZFS were also performed in order to clearly see the difference to the simulations with the ZFS. For the simulations without the ZFS, the modulation depth of the LaserIMD simulations with the ZFS was taken as it was determined by the fit and reduced by a factor of 2/3, because the coherence transfer pathway with $\Delta m_T = 0$ no longer contributes to the echo modulation.

25
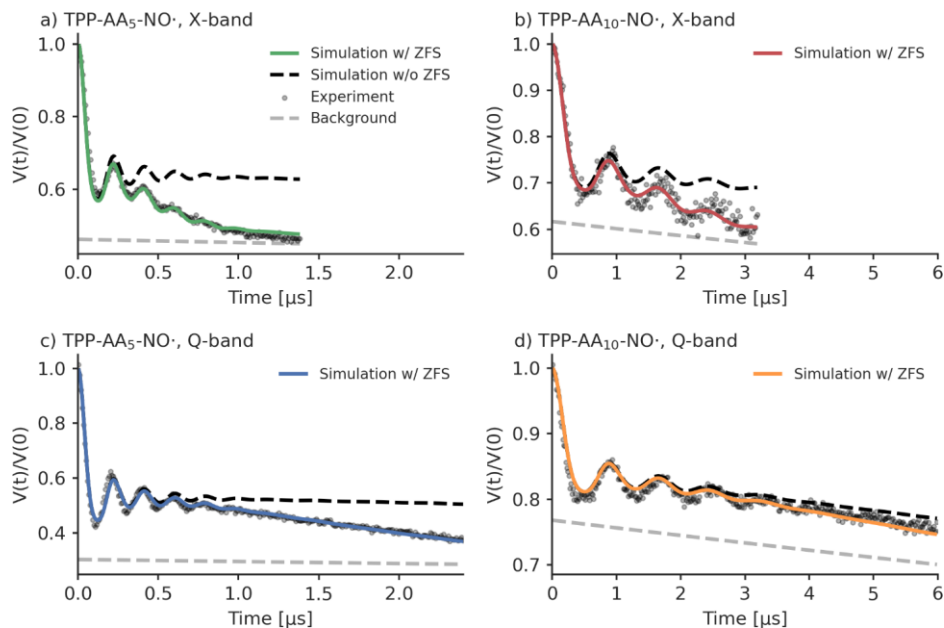
Figure 12~~10~~: Experimental LaserIMD traces of the peptides, recorded at 30 K in MeOD/D$_2$O (98/2 vol.%). a) TPP-AA$_5$-NO• in X-band ($\omega\nu_{T\ell} = 9.28$ **GHz**) (green), b) TPP-AA$_{10}$-NO• in X-band ($\nu\omega_T = 9.31$ GHz) (red), c) TPP-AA$_5$-NO• in Q-band ($\nu\omega_T = 34.00$ GHz) (blue), d) TPP-AA$_{10}$-NO• in Q-band ($\nu\omega_T = 34.00$ GHz) (orange). The colored traces show simulations that include the ZFS. The simulations without the effects of the ZFS are shown as black dashed line. The experimentally recorded data are depicted as grey dots. The backgrounds of the simulations are shown as grey dashed line. The simulations were performed with the distance distributions and background decays that were obtained by the LiDEER measurements.

The results of the LaserIMD measurements and the corresponding simulations are shown in Figure 12~~Fig. 10~~. It can be clearly seen that the shape of the experimental traces changes depending on whether they were recorded in X- or Q-band and with those with a stronger decay in X-band. This is a first strong indication of the effect of the ZFS, as predicted by the simulations (see Figure 5~~Fig. 5~~). The influence of the ZFS shows itself clearly in the differences between the experimental data and the simulations where the effect of the ZFS was ignored. In particular, the experimental LaserIMD traces show a stronger decay than the background decay of simulations without the ZFS. This difference is more pronounced in TPP-AA$_5$-NO• than in TPP-AA$_{10}$-NO• and also stronger in X-band than in Q-band. Thus, for TPP-AA$_5$-NO• in X-band, the deviation between the simulations without the ZFS and the experiments is the largest, whereas in the case of TPP-AA$_{10}$-NO• in Q-band, it is nearly absent. This additional decay of the experimental traces cannot be explained without considering the effect of the ZFS, but is

Formatiert: Rechtschreibung und Grammatik prüfen

properly understandable with a model that includes the ZFS. The stronger decay of the experimental traces can be assigned to the coherence transfer pathway with $\Delta m_T = 0$, which leads to an additional contribution to the LaserIMD trace $V_0^{non-sec}(t)$ with a continuously decaying signal (see Figure 4~~Fig. 4~~). As shorter distances and lower magnetic fields lead to a stronger decay of $V_0^{non-sec}(t)$, this also explains why the additional decay in the experimental data is stronger for TPP-AA$_5$-NO• than

5 for TPP-AA$_{10}$-NO• and stronger in X- than in Q-band. It is noteworthy that the model with the ZFS provides not only a qualitative but also a quantitative agreement between the experimentally recorded LaserIMD traces and the corresponding simulations.

To see how the additional decay of the ZFS affects the analysis of experimental LaserIMD traces, the recorded data were analyzed with Tikhonov regularization; and the results that are obtained with a LaserIMD kernel that includes the ZFS are

10 compared to those obtained by a DEER kernel that ignores the ZFS (see S11 for a detailed overview of the results). The comparison of the obtained distance distributions shows that, even when the ZFS is ignored, the main distance peak is obtained correctly in all cases. For the measurements in Q-band, the entire distance distributions turn out to be virtually identical, regardless whether the ZFS is included in the analysis routine or not (see Fig. S13c-d). The situation is different in X-band. For TPP-AA$_5$-NO• in X-band, the strong additional decay is interpreted as an additional artifact peak at around 5.0 nm if the

15 ZFS is ignored (see Fig. S13a). This peak disappears when the ZFS is considered. For TPP-AA$_{10}$-NO• in X-band, the analysis which ignores the ZFS also shows an additional peak around 7.0 nm. However, this artifact is not as pronounced as the one of TPP-AA$_5$-NO• and disappears in the validation. For the modulation depths and the background decay rates, there are notable differences when the ZFS is considered or not (see Table S5 and S6 in S11). In all cases, ignoring the ZFS leads to a reduced modulation depth. In Q-band, the modulation depth is reduced by a factor of $\approx 2/3$ which means that the additional decay is

20 completely assigned to the intermolecular background. In accordance with that, the background decay rates are larger when the ZFS is ignored. In X-band, these effects are not so pronounced. As the additional decay is partially fitted by introducing distance artifacts when ignoring the ZFS, the modulation depth is reduced only by a factor of 0.72 for TPP-AA$_{10}$-NO• and 0.84 for TPP-AA$_5$-NO•.

These results show that ignoring the ZFS for the analysis of LaserIMD leads to artifacts in the obtained results. For TPP as

25 transient spin label, the artifacts are not so prominent in Q-band. There, the additional decay mostly leads to a stronger background decay and reduced modulation depth and the distance distribution remains virtually unchanged. In X-band, however, artifact peaks in the distance distribution can occur if the ZFS is ignored.

5 Conclusion and Outlook

In light-induced PDS, the ZFS interaction of the transient triplet label is a crucial parameter that can alter the shape of the

30 dipolar traces. This implies that in contrast to the former assumption, the spin system in LaserIMD and LiDEER cannot be treated in the secular approximation where the spin system~~s~~ behaves as if it would consist of two $S = 1/2$ spins. A theoretical description of LaserIMD and LiDEER that also includes non-secular terms was developed and it was shown that the dipolar

frequencies depend on the magnitude of the ZFS and the Zeeman frequency (i.e. the external magnetic field). Time-domain simulations showed that in LiDEER, this effects of the ZFS can be suppressed by exciting either of the $Y^{\pm}$ peaks with the observer pulses and by using transient triplet labels whose ZFS is small compared to the Zeeman frequency, like e.g. TPP in Q-band. For experimental LiDEER data which are recorded under such conditions the effect of the ZFS is negligible and a

5   standard DEER kernel that does not consider the ZFS can be employed for data analysis.

In LaserIMD, simulations as well as experiments confirmed that there is an influence of the ZFS on the dipolar trace. It virtually does not affect the dipolar oscillation of the coherence transfer pathways with $\Delta m_{\mathrm{T}} = \pm 1$, but is manifested in an additional decay of the LaserIMD trace. This decay is caused by the third coherence transfer pathway with $\Delta m_{\mathrm{T}} = 0$, which was formerly believed not to contribute to the signal. The strength of this additional decay primarily depends on the ratio of the ZFS to the

10 Zeeman frequency and also the distance between the transient and permanent spin label: It is stronger for larger ZFS, lower magnetic fields and shorter distances. A software tool for the calculation of LaserIMD kernels that take the influence of the ZFS into account was developed. It is available at github (https://github.com/andreas-scherer/LaserIMD_kernel) and allows to specify different ZFS values, zero-field populations and Zeeman frequencies. The feasibility of the new kernel was proven by experimentally recorded LaserIMD traces. A DEER kernel which ignores the ZFS cannot fit these traces correctly and strong

15 derivations between the experimental data and simulations can be observed. However, Wwith the newly developed model that considers the ZFS, however, excellent fits of the experimental data were produced. The analysis of the experimental and simulated LaserIMD data with Tikhonov regularization showed that ignoring the ZFS compromises the obtained results. For transient triplet labels with a ZFS of $\approx$ 1 GHz like TPP, this is no so problematic in Q-band. There, only the obtained modulation depths and background decay rates are affected if the ZFS is ignored; the distance distribution remains unchanged.

20 In X-band, however, ignoring the ZFS is more severe and can additionally lead to artifact peaks in the distance distributions. This shows that the ZFS can have a significant impact in LaserIMD and should be considered when experimental data are analyzed.

6 Data availability

The raw data can be downloaded at https://doi.org/10.5281/zenodo.7283499.

7 Code availability

The source code for the LaserIMD kernel can be downloaded at https://github.com/andreas-scherer/LaserIMD_kernel. The source code for the time-domain LiDEER simulations can be downloaded at https://github.com/andreas-scherer/LiDEER_simulations.git

8 Author contribution

AS and MD conceived the research idea and designed the simulations and experiments. AS performed the analytical calculations and AS and BY conducted the simulations and experiments and analyzed the results. AS prepared all the figures and wrote the draft manuscript. All authors discussed the results and revised the manuscript.

9 Competing interests

The authors declare no conflict of interests.

10 Acknowledgements

11 References

Abdullin, D., Matsuoka, H., Yulikov, M., Fleck, N., Klein, C., Spicher, S., Hagelueken, G., Grimme, S., Luetzen, A., and Schiemann, O.: Pulsed EPR Dipolar Spectroscopy under the Breakdown of the High-Field Approximation: The High-Spin Iron(III) Case, Chem. Eur. J., 0, https://doi.org/10.1002/chem.201900977, 2019.

5 Bak, M. and Nielsen, N. C.: REPULSION, A Novel Approach to Efficient Powder Averaging in Solid-State NMR, Semi-Rigid Nitroxide Spin Label for Long-Range EPR Distance Measurements of Lipid Bilayer Embedded β-Peptides, 125, 132–139, https://doi.org/10.1006/jmre.1996.1087, 1997.

Bertran, A., Henbest, K. B., De Zotti, M., Gobbo, M., Timmel, C. R., Di Valentin, M., and Bowen, A. M.: Light-Induced Triplet–Triplet Electron Resonance Spectroscopy, J. Phys. Chem. Lett., 80–85, https://doi.org/10.1021/acs.jpclett.0c02884, 10   2020.

Bertran, A., Barbon, A., Bowen, A. M., and Di Valentin, M.: Chapter Seven - Light-induced pulsed dipolar EPR spectroscopy for distance and orientation analysis, in: Methods in Enzymology, vol. 666, edited by: Britt, R. D., Academic Press, 171–231, https://doi.org/10.1016/bs.mie.2022.02.012, 2022a.

Bertran, A., Morbiato, L., Aquilia, S., Gabbatore, L., De Zotti, M., Timmel, C. R., Di Valentin, M., and Bowen, A. M.: 15   Erythrosin B as a New Photoswitchable Spin Label for Light-Induced Pulsed EPR Dipolar Spectroscopy, Molecules, 27, 7526, https://doi.org/10.3390/molecules27217526, 2022b.

Bieber, A., Bücker, D., and Drescher, M.: Light-induced dipolar spectroscopy – A quantitative comparison between LiDEER and LaserIMD, J. Magn. Reson., 296, 29–35, https://doi.org/10.1016/j.jmr.2018.08.006, 2018.

Bowen, A. M., Bertran, A., Henbest, K. B., Gobbo, M., Timmel, C. R., and Di Valentin, M.: Orientation-Selective and 20   Frequency-Correlated Light-Induced Pulsed Dipolar Spectroscopy, J. Phys. Chem. Lett., 12, 3819–3826, https://doi.org/10.1021/acs.jpclett.1c00595, 2021.

Bowman, M. K., Maryasov, A. G., Kim, N., and DeRose, V. J.: Visualization of distance distribution from pulsed double electron-electron resonance data, Applied Magnetic Resonance, 26, 23, https://doi.org/10.1007/BF03166560, 2004.

Bücker, D., Sickinger, A., Ruiz Perez, J. D., Oestringer, M., Mecking, S., and Drescher, M.: Direct Observation of Chain 25   Lengths and Conformations in Oligofluorene Distributions from Controlled Polymerization by Double Electron–Electron Resonance, J. Am. Chem. Soc., https://doi.org/10.1021/jacs.9b11404, 2019.

Collauto, A., von Bülow, S., Gophane, D. B., Saha, S., Stelzl, L. S., Hummer, G., Sigurdsson, S. T., and Prisner, T. F.: Compaction of RNA Duplexes in the Cell, Angew. Chem., Int. Ed., n/a, https://doi.org/10.1002/anie.202009800, 2020.

Dal Farra, M. G., Richert, S., Martin, C., Larminie, C., Gobbo, M., Bergantino, E., Timmel, C. R., Bowen, A. M., and Di 30   Valentin, M.: Light-induced pulsed EPR dipolar spectroscopy on a paradigmatic Hemeprotein, ChemPhysChem, 0, https://doi.org/10.1002/cphc.201900139, 2019a.

Dal Farra, M. G., Ciuti, S., Gobbo, M., Carbonera, D., and Di Valentin, M.: Triplet-state spin labels for highly sensitive pulsed dipolar spectroscopy, Mol. Phys., 117, 2673–2687, https://doi.org/10.1080/00268976.2018.1503749, 2019b.

Dalaloyan, A., Qi, M., Ruthstein, S., Vega, S., Godt, A., Feintuch, A., and Goldfarb, D.: Gd(iii)-Gd(iii) EPR distance measurements - the range of accessible distances and the impact of zero field splitting, Phys. Chem. Chem. Phys., 17, 18464–18476, https://doi.org/10.1039/C5CP02602D, 2015.

Di Valentin, M., Albertini, M., Zurlo, E., Gobbo, M., and Carbonera, D.: Porphyrin Triplet State as a Potential Spin Label for

5   Nanometer Distance Measurements by PELDOR Spectroscopy, J. Am. Chem. Soc., 136, 6582–6585, https://doi.org/10.1021/ja502615n, 2014.

Di Valentin, M., Albertini, M., Dal Farra, M. G., Zurlo, E., Orian, L., Polimeno, A., Gobbo, M., and Carbonera, D.: Light-Induced Porphyrin-Based Spectroscopic Ruler for Nanometer Distance Measurements, Chem. Eur. J., 22, 17204–17214, https://doi.org/10.1002/chem.201603666, 2016.

10   Edwards, T. H. and Stoll, S.: Optimal Tikhonov regularization for DEER spectroscopy, J. Magn. Reson., 288, 58–68, https://doi.org/10.1016/j.jmr.2018.01.021, 2018.

Fábregas Ibáñez, L., Jeschke, G., and Stoll, S.: DeerLab: A comprehensive toolbox for analyzing dipolar EPR spectroscopy data, Magn. Reson. Discuss., 2020, 1–28, https://doi.org/10.5194/mr-2020-13, 2020.

García-Rubio, I.: EPR of site-directed spin-labeled proteins: A powerful tool to study structural flexibility, Arch. Biochem.

15   Biophys., 684, 108323, https://doi.org/10.1016/j.abb.2020.108323, 2020.

Giannoulis, A., Feintuch, A., Barak, Y., Mazal, H., Albeck, S., Unger, T., Yang, F., Su, X.-C., and Goldfarb, D.: Two closed ATP- and ADP-dependent conformations in yeast Hsp90 chaperone detected by Mn(II) EPR spectroscopic techniques, Proc. Natl. Acad. Sci. U.S.A., 117, 395, https://doi.org/10.1073/pnas.1916030116, 2020.

Hagston, W. E. and Holmes, B. J.: Matrix methods for spin Hamiltonians of low symmetry, J. Phys. B: Atom. Mol. Phys., 13,

20   3505–3519, https://doi.org/10.1088/0022-3700/13/18/005, 1980.

Hintze, C., Schutze, F., Drescher, M., and Mecking, S.: Probing of chain conformations in conjugated polymer nanoparticles by electron spin resonance spectroscopy, Phys. Chem. Chem. Phys., 17, 32289–32296, https://doi.org/10.1039/C5CP05749C, 2015.

Hintze, C., Bücker, D., Domingo Köhler, S., Jeschke, G., and Drescher, M.: Laser-Induced Magnetic Dipole Spectroscopy, J.

25   Phys. Chem. Lett., 7, 2204–2209, https://doi.org/10.1021/acs.jpclett.6b00765, 2016.

Hogben, H. J., Krzystyniak, M., Charnock, G. T. P., Hore, P. J., and Kuprov, I.: Spinach – A software library for simulation of spin dynamics in large spin systems, J. Magn. Reson., 208, 179–194, https://doi.org/10.1016/j.jmr.2010.11.008, 2011.

Hu, P. and Hartmann, S. R.: Theory of spectral diffusion decay using an uncorrelated-sudden-jump model, Phys. Rev. B, 9, 1–13, https://doi.org/10.1103/PhysRevB.9.1, 1974.

30   Hubbell, W. L., López, C. J., Altenbach, C., and Yang, Z.: Technological advances in site-directed spin labeling of proteins, Current Opinion in Structural Biology, 23, 725–733, https://doi.org/10.1016/j.sbi.2013.06.008, 2013.

Jeschke, G.: DEER Distance Measurements on Proteins, Annu. Rev. Phys. Chem., 63, 419–446, https://doi.org/10.1146/annurev-physchem-032511-143716, 2012.

Jeschke, G., Panek, G., Godt, A., Bender, A., and Paulsen, H.: Data analysis procedures for pulse ELDOR measurements of broad distance distributions, Appl. Magn. Reson., 26, 223, https://doi.org/10.1007/BF03166574, 2004.

Jeschke, G., Chechik, V., Ionita, P., Godt, A., Zimmermann, H., Banham, J., Timmel, C. R., Hilger, D., and Jung, H.: DeerAnalysis2006 - a comprehensive software package for analyzing pulsed ELDOR data, Appl. Magn. Reson., 30, 473–498, https://doi.org/10.1007/BF03166213, 2006.

Jeschke, G., Sajid, M., Schulte, M., Ramezanian, N., Volkov, A., Zimmermann, H., and Godt, A.: Flexibility of Shape-Persistent Molecular Building Blocks Composed of p-Phenylene and Ethynylene Units, J. Am. Chem. Soc., 132, 10107–10117, https://doi.org/10.1021/ja102983b, 2010.

Keeley, J., Choudhury, T., Galazzo, L., Bordignon, E., Feintuch, A., Goldfarb, D., Russell, H., Taylor, M. J., Lovett, J. E., Eggeling, A., Fabregas Ibanez, L., Keller, K., Yulikov, M., Jeschke, G., and Kuprov, I.: Neural networks in pulsed dipolar spectroscopy: a practical guide, J. Magn. Reson., 107186, https://doi.org/10.1016/j.jmr.2022.107186, 2022.

Krumkacheva, O. A., Timofeev, I. O., Politanskaya, L. V., Polienko, Y. F., Tretyakov, E. V., Rogozhnikova, O. Yu., Trukhin, D. V., Tormyshev, V. M., Chubarov, A. S., Bagryanskaya, E. G., and Fedin, M. V.: Triplet Fullerenes as Prospective Spin Labels for Nanoscale Distance Measurements by Pulsed Dipolar EPR, Angew. Chem., Int. Ed., 585, 13271–13275, https://doi.org/10.1002/ange.201904152, 2019.

Marko, A., Denysenkov, V., Margraf, D., Cekan, P., Schiemann, O., Sigurdsson, S. Th., and Prisner, T. F.: Conformational Flexibility of DNA, J. Am. Chem. Soc., 133, 13375–13379, https://doi.org/10.1021/ja201244u, 2011.

Marko, A., Denysenkov, V., and Prisner, T. F.: Out-of-phase PELDOR, Molecular Physics, 111, 2834–2844, https://doi.org/10.1080/00268976.2013.807369, 2013.

Maryasov, A. G., Bowman, M. K., and Tsvetkov, Yu. D.: Dipole-dipole interactions of high-spin paramagnetic centers in disordered systems, Appl. Magn. Reson., 30, 683, https://doi.org/10.1007/BF03166227, 2006.

Milov, A. D., Salikhov, K. M., and Shirov, M. D.: Use of the double resonance in electron spin echo method for the study of paramagnetic center spatial distribution in solids., Fiz. Tverd. Tela, 23, 975–982, 1981.

Milov, A. D., Ponomarev, A. B., and Tsvetkov, Yu. D.: Electron-electron double resonance in electron spin echo: Model biradical systems and the sensitized photolysis of decalin, Chem. Phys. Lett., 110, 67–72, https://doi.org/10.1016/0009-2614(84)80148-7, 1984.

Milov, A. D., Maryasov, A. G., and Tsvetkov, Y. D.: Pulsed electron double resonance (PELDOR) and its applications in free-radicals research, Appl. Magn. Reson., 15, 107–143, https://doi.org/10.1007/BF03161886, 1998.

Pake, G. E.: Nuclear Resonance Absorption in Hydrated Crystals: Fine Structure of the Proton Line, J. Chem. Phys., 16, 327–336, https://doi.org/10.1063/1.1746878, 1948.

Pannier, M., Veit, S., Godt, A., Jeschke, G., and Spiess, H. W.: Dead-Time Free Measurement of Dipole–Dipole Interactions between Electron Spins, J. Magn. Reson., 142, 331–340, https://doi.org/10.1006/jmre.1999.1944, 2000.

Ritsch, I., Lehmann, E., Emmanouilidis, L., Yulikov, M., Allain, F., and Jeschke, G.: Phase Separation of Heterogeneous Nuclear Ribonucleoprotein A1 upon Specific RNA-Binding Observed by Magnetic Resonance, Angew. Chem., Int. Ed., n/a, https://doi.org/10.1002/anie.202204311, 2022.

Robotta, M., Gerding, H. R., Vogel, A., Hauser, K., Schildknecht, S., Karreman, C., Leist, M., Subramaniam, V., and Drescher,
5 M.: Alpha-Synuclein Binds to the Inner Membrane of Mitochondria in an α-Helical Conformation, ChemBioChem, 15, 2499–2502, https://doi.org/10.1002/cbic.201402281, 2014.

Rose, M. E.: Elementary theory of angular momentum, Courier Corporation, 1995.

Roser, P., Schmidt, M. J., Drescher, M., and Summerer, D.: Site-directed spin labeling of proteins for distance measurements in vitro and in cells, Org. Biomol. Chem., 14, 5468–5476, https://doi.org/10.1039/C6OB00473C, 2016.

10 Scherer, A., Yao, X., Qi, M., Wiedmaier, M., Godt, A., and Drescher, M.: Increasing the Modulation Depth of Gd(III)-Based Pulsed Dipolar EPR Spectroscopy (PDS) with Porphyrin-Gd(III) Laser-Induced Magnetic Dipole Spectroscopy, J. Phys. Chem. Lett., 13, 10958–10964, https://doi.org/10.1021/acs.jpclett.2c02138, 2022.

Schweiger, A. and Jeschke, G.: Principles of Pulse Electron Paramagnetic Resonance, Oxford University Press on Demand, 2001.

15 Serrer, K., Matt, C., Sokolov, M., Kacprzak, S., Schleicher, E., and Weber, S.: Application of commercially available fluorophores as triplet spin probes in EPR spectroscopy, Mol. Phys., 117, 2688–2699, https://doi.org/10.1080/00268976.2019.1608379, 2019.

Tait, C. E. and Stoll, S.: Coherent pump pulses in Double Electron Electron Resonance spectroscopy, Phys. Chem. Chem. Phys., 18, 18470–18485, https://doi.org/10.1039/C6CP03555H, 2016.

20 Takeda, K., Takegoshi, K., and Terao, T.: Dynamic nuclear polarization by electron spins in the photoexcited triplet state: I. Attainment of proton polarization of 0.7 at 105 K in naphthalene, Journal of the Physical Society of Japan, 73, 2313–2318, 2004.

Telser, J.: EPR Interactions–Zero-Field Splittings, eMagRes, 6, 207–234, 2017.

Timofeev, I. O., Politanskaya, L. V., Tretyakov, E. V., Polienko, Y. F., Tormyshev, V. M., Bagryanskaya, E., Krumkacheva,
25 O. A., and Fedin, M. V.: Fullerene-based triplet spin labels: methodology aspects for pulsed dipolar EPR spectroscopy, Phys. Chem. Chem. Phys., 4475–4484, https://doi.org/10.1039/D1CP05545C, 2022.

Wasielewski, M. R., O'Neil, M. P., Lykke, K. R., Pellin, M. J., and Gruen, D. M.: Triplet states of fullerenes C60 and C70. Electron paramagnetic resonance spectra, photophysics, and electronic structures, Journal of the American Chemical Society, 113, 2774–2776, 1991.

30 Weickert, S., Wawrzyniuk, M., John, L. H., Rüdiger, S. G. D., and Drescher, M.: The mechanism of Hsp90-induced oligomerizaton of Tau, Sci Adv, 6, eaax6999, https://doi.org/10.1126/sciadv.aax6999, 2020.

Williams, L., Tischlik, S., Scherer, A., Fischer, J. W. A., and Drescher, M.: Site-directed attachment of photoexcitable spin labels for light-induced pulsed dipolar spectroscopy, Chem. Commun., 56, 14669–14672, https://doi.org/10.1039/D0CC03101A, 2020.

Wojciechowski, F., Groß, A., Holder, I. T., Knörr, L., Drescher, M., and Hartig, J. S.: Pulsed EPR spectroscopy distance measurements of DNA internally labelled with Gd3+-DOTA, Chem. Commun., 51, 13850–13853, https://doi.org/10.1039/C5CC04234H, 2015.

Worswick, S. G., Spencer, J. A., Jeschke, G., and Kuprov, I.: Deep neural network processing of DEER data, Sci Adv, 4,
5   https://doi.org/10.1126/sciadv.aat5218, 2018.

Yang, Y., Chen, S.-N., Yang, F., Li, X.-Y., Feintuch, A., Su, X.-C., and Goldfarb, D.: In-cell destabilization of a homodimeric protein complex detected by DEER spectroscopy, Proc Natl Acad Sci USA, 117, 20566–20575, https://doi.org/10.1073/pnas.2005779117, 2020.

Yee, E. F., Diensthuber, R. P., Vaidya, A. T., Borbat, P. P., Engelhard, C., Freed, J. H., Bittl, R., Möglich, A., and Crane, B.
10 R.: Signal transduction in light–oxygen–voltage receptors lacking the adduct-forming cysteine residue, Nat. Commun., 6, 10079, https://doi.org/10.1038/ncomms10079, 2015.

Supporting Information of

The effect of the zero-field splitting ~~interaction~~ in light-induced pulsed dipolar EPR spectroscopy

5 Andreas Scherer, Berk, Yildirim, Malte Drescher

Department of Chemistry and Konstanz Research School Chemical Biology, University of Konstanz, 78457 Konstanz, Germany

Correspondence to: Malte Drescher (malte.drescher@uni-konstanz.de)

10

15

20

1

Table of contents

S1 Theoretical derivation

The Hamiltonian is a sum of the secular and non-secular parts:

$$\hat{H} = \hat{H}^{\text{sec}} + \hat{H}^{\text{non-sec}}, \tag{S1}$$

With

$$\hat{H}^{\text{sec}} = 2\pi\omega\nu_D\hat{S}_{D,z} + 2\pi\omega\nu_T\hat{S}_{T,z} + \left(\frac{D(3\cos^2(\beta_T) - 1)}{6} + \frac{E\sin^2(\beta_T)\cos(2\gamma_T)}{2}\right)\left(2\hat{S}_{T,z}\hat{S}_{T,z} - \left(\hat{S}_{T,x}\hat{S}_{T,x} + \hat{S}_{T,y}\hat{S}_{T,y}\right)\right)$$
$$+ \omega_{\text{dip}}(3\cos^2\beta_{\text{dip}} - 1)\hat{S}_{D,z}\hat{S}_{T,z} \tag{S2}$$

$$\hat{H}^{\text{non-sec}} = \left(\frac{D\sin 2\beta_T\exp(-i\alpha_T)}{4} - \frac{E\sin(\beta_T)(\cos(\beta_T)\cos(2\gamma_T) - i\sin(2\gamma_T))\exp(-i\alpha_T)}{2}\right)\left(\hat{S}_{T,z}\hat{S}_{T,+} + \hat{S}_{T,+}\hat{S}_{T,z}\right)$$
$$+ \left(\frac{D\sin 2\beta_T\exp(i\alpha_T)}{4} - \frac{E\sin(\beta_T)(\cos(\beta_T)\cos(2\gamma_T) + i\sin(2\gamma_T))\exp(i\alpha_T)}{2}\right)\left(\hat{S}_{T,-}\hat{S}_{T,z} + \hat{S}_{T,-}\hat{S}_{T,z}\right) \tag{S3}$$
$$+ \frac{3\omega_{\text{dip}}\sin 2\beta_{\text{dip}}}{4}\hat{S}_{D,z}\hat{S}_{T,+} + \frac{3\omega_{\text{dip}}\sin 2\beta_{\text{dip}}}{4}\hat{S}_{D,z}\hat{S}_{T,-}$$

~~Here, $\hat{S}_{T,+}$ and $\hat{S}_{D,+}$ are the raising ($\hat{S}_+ = \hat{S}_x + i\hat{S}_y$) and $\hat{S}_{D,-}$ and $\hat{S}_{T,-}$ are the lowering ($\hat{S}_- = \hat{S}_x - i\hat{S}_y$) operators. Note that this non-secular part does not include all non-secular terms and all pseudo-secular terms are also ignored here. As is shown in S2 these remaining terms have only a negligible effect at the magnetic fields strengths that are relevant in most experiments, and this is why they can be left out.~~ The secular Hamiltonian is already diagonal with the eigenvalues $E^{\text{sec}}_{m_D, m_T}$ (Abragam and Bleaney, 2012; Blank and Levanon, 2005):

$$E^{\text{sec}}_{+\frac{1}{2}, +1} = \frac{\omega_D}{2} + \omega_T + E^{\text{sec}}_{\text{ZFS}} + E^{\text{sec}}_{\text{dip}}, \tag{S4}$$

$$E^{\text{sec}}_{+\frac{1}{2}, 0} = \frac{\omega_{Ds}}{2} - 2E^{\text{sec}}_{\text{ZFS}}, \tag{S5}$$

$$E^{\text{sec}}_{+\frac{1}{2}, -1} = \frac{\omega_D}{2} - \omega_T + E^{\text{sec}}_{\text{ZFS}} - E^{\text{sec}}_{\text{dip}}, \tag{S6}$$

$$E^{\text{sec}}_{-\frac{1}{2}, +1} = -\frac{\omega_D}{2} + \omega_T + E^{\text{sec}}_{\text{ZFS}} - E^{\text{sec}}_{\text{dip}}, \tag{S7}$$

$$E^{\text{sec}}_{-\frac{1}{2}, 0} = -\frac{\omega_D}{2} - 2E^{\text{sec}}_{\text{ZFS}}, \tag{S8}$$

$$E^{\text{sec}}_{-\frac{1}{2}, -1} = -\frac{\omega_D}{2} - \omega_T + E^{\text{sec}}_{\text{ZFS}} + E^{\text{sec}}_{\text{dip}}. \tag{S9}$$

Here, the following abbreviations were used:

$$E^{\text{sec}}_{\text{ZFS}} = \frac{3\cos(\beta_T)^2 - 1}{6}D + \frac{\cos(2\gamma_T)\sin(\beta_T)^2}{2}E \tag{S10}$$

and

$$E^{\text{sec}}_{\text{dip}} = \frac{3\cos(\beta_{\text{dip}})^2 - 1}{2}\omega_{\text{dip}}. \tag{S11}$$

The non-secular terms contribute the following off-diagonal elements to the Hamiltonian:

3

$$\langle +\tfrac{1}{2},+1|\widehat{H}^{\text{non-sec}}|+\tfrac{1}{2},0\rangle = H_{\text{ZFS}}^{\text{non-sec}} + H_{\text{dip}}^{\text{non-sec}}, \tag{S12}$$

$$\langle +\tfrac{1}{2},0|\widehat{H}^{\text{non-sec}}|+\tfrac{1}{2},-1\rangle = -H_{\text{ZFS}}^{\text{non-sec}} + H_{\text{dip}}^{\text{non-sec}}, \tag{S13}$$

$$\langle -\tfrac{1}{2},+1|\widehat{H}^{\text{non-sec}}|-\tfrac{1}{2},0\rangle = H_{\text{ZFS}}^{\text{non-sec}} - H_{\text{dip}}^{\text{non-sec}}, \tag{S14}$$

$$\langle -\tfrac{1}{2},0|\widehat{H}^{\text{non-sec}}|-\tfrac{1}{2},-1\rangle = -H_{\text{ZFS}}^{\text{non-sec}} - H_{\text{dip}}^{\text{non-sec}}, \tag{S15}$$

With the following abbreviations

$$E_{\text{ZFS}}^{\text{non-sec}} = \frac{\sqrt{2}\sin(2\beta_{\text{T}})\exp(-i\alpha_{\text{T}})}{4} D - \frac{\sin(\beta_{\text{T}})(\cos(\beta_{\text{T}})\cos(2\gamma_{\text{T}})-i\sin(2\gamma_{\text{T}}))\exp(-i\alpha_{\text{T}})}{\sqrt{2}} E \tag{S16}$$

and

$$E_{\text{dip}}^{\text{non-sec}} = \frac{3\sqrt{2}\sin(2\beta_{\text{dip}})}{8}\omega_{\text{dip}}. \tag{S17}$$

Written in matrix-form, the full Hamiltonian is:

$$\widehat{H} = \widehat{H}^{\text{sec}} + \widehat{H}^{\text{non-sec}} = \begin{pmatrix} \hat{A} & 0 \\ 0 & \hat{B} \end{pmatrix} \tag{S18}$$

$$\hat{A} = \begin{pmatrix} E_{+\frac{1}{2},+1}^{\text{sec}} & E_{\text{ZFS}}^{\text{non-sec}} + E_{\text{dip}}^{\text{non-sec}} & 0 \\ \bar{E}_{\text{ZFS}}^{\text{non-sec}} + E_{\text{dip}}^{\text{non-sec}} & E_{+\frac{1}{2},0}^{\text{sec}} & -E_{\text{ZFS}}^{\text{non-sec}} + E_{\text{dip}}^{\text{non-sec}} \\ 0 & -\bar{E}_{\text{ZFS}}^{\text{non-sec}} + \bar{E}_{\text{dip}}^{\text{non-sec}} & E_{+\frac{1}{2},-1}^{\text{sec}} \end{pmatrix}, \tag{S19}$$

$$\hat{B} = \begin{pmatrix} E_{-\frac{1}{2},+1}^{\text{sec}} & E_{\text{ZFS}}^{\text{non-sec}} - E_{\text{dip}}^{\text{non-sec}} & 0 \\ \bar{E}_{\text{ZFS}}^{\text{non-sec}} - \bar{E}_{\text{dip}}^{\text{non-sec}} & E_{-\frac{1}{2},0}^{\text{sec}} & -E_{\text{ZFS}}^{\text{non-sec}} - E_{\text{dip}}^{\text{non-sec}} \\ 0 & -\bar{E}_{\text{ZFS}}^{\text{non-sec}} - \bar{E}_{\text{dip}}^{\text{non-sec}} & E_{-\frac{1}{2},-1}^{\text{sec}} \end{pmatrix}. \tag{S20}$$

To calculate the eigenvalues of this Hamiltonian perturbation theory was used. $\widehat{H}^{\text{non-sec}}$ only includes off-diagonal elements, so the first order corrections are zero. The second order corrections were calculated according to:

$$E_{m_{\text{D}},m_{\text{T}}}^{\text{non-sec}} = E_{m_{\text{D}},m_{\text{T}}}^{\text{sec}} + \sum_{m_{\text{D}},m_{\text{T}} \neq m'_{\text{D}},m'_{\text{T}}} \frac{\left|\langle m_{\text{D}},m_{\text{T}}|\widehat{H}^{\text{non-sec}}|m'_{\text{D}},m'_{\text{T}}\rangle\right|^2}{E_{m_{\text{D}},m_{\text{T}}}^{\text{sec}} - E_{m'_{\text{D}},m'_{\text{T}}}^{\text{sec}}} \tag{S21}$$

For further simplification, energy difference of two adjacent levels of the triplet submanifolds were simplified to only include the Zeeman splitting:

$$E_{\pm\frac{1}{2},+1}^{\text{sec}} - E_{\pm\frac{1}{2},0}^{\text{sec}} \approx E_{\pm\frac{1}{2},0}^{\text{sec}} - E_{\pm\frac{1}{2},-1}^{\text{sec}} \approx 2\pi\omega\nu_{\text{T}} \tag{S22}$$

The second order corrections result in the following eigenvalues:

$$E_{+\frac{1}{2},+1}^{\text{non-sec}} = E_{+\frac{1}{2},+1}^{\text{sec}} + \frac{\left|\langle+\frac{1}{2},+1|\hat{H}^{\text{non-sec}}|+\frac{1}{2},\,0\rangle\right|^2}{2\pi\nu\omega_{\text{T}}} = \frac{|E_{\text{ZFS}}^{\text{non-sec}}|^2 + 2\text{Re}(E_{\text{ZFS}}^{\text{non-sec}})\cdot E_{\text{d}}^{\text{non-sec}} + E_{\text{d}}^{\text{non-sec}\,2}}{2\pi\omega\nu_{\text{T}}}, \tag{S23}$$

$$E_{+\frac{1}{2},0}^{\text{non-sec}} = E_{+\frac{1}{2},0}^{\text{sec}} - \frac{\left|\langle+\frac{1}{2},+1|\hat{H}^{\text{non-sec}}|+\frac{1}{2},\,0\rangle\right|^2}{2\pi\nu_{\text{T}}\omega_{\text{T}}} + \frac{\left|\langle+\frac{1}{2},0|\hat{H}^{\text{non-sec}}|+\frac{1}{2},\,-1\rangle\right|^2}{2\pi\nu_{\text{T}}\omega_{\text{T}}} = -4\frac{E_{\text{ZFS}}^{\text{non-sec}}\cdot E_{\text{dip}}^{\text{non-sec}}}{2\pi\nu_{\text{T}}\omega_{\text{T}}}, \tag{S24}$$

$$E_{+\frac{1}{2},-1}^{\text{non-sec}} = E_{+\frac{1}{2},-1}^{\text{sec}} - \frac{\left|\langle+\frac{1}{2},0|\hat{H}^{\text{non-sec}}|+\frac{1}{2},\,-1\rangle\right|^2}{2\pi\nu_{\text{T}}\omega_{\text{T}}} = -\frac{|E_{\text{ZFS}}^{\text{non-sec}}|^2 - 2\text{Re}(E_{\text{ZFS}}^{\text{non-sec}})\cdot E_{\text{dip}}^{\text{non-sec}} + E_{\text{dip}}^{\text{non-sec}\,2}}{2\pi\nu_{\text{T}}\omega_{\text{T}}}, \tag{S25}$$

$$E_{-\frac{1}{2},+1}^{\text{non-sec}} = E_{-\frac{1}{2},+1}^{\text{sec}} + \frac{\left|\langle-\frac{1}{2},+1|\hat{H}^{\text{non-sec}}|-\frac{1}{2},\,0\rangle\right|^2}{2\pi\nu_{\text{T}}\omega_{\text{T}}} = \frac{|E_{\text{ZFS}}^{\text{non-sec}}|^2 - 2\text{Re}(E_{\text{ZFS}}^{\text{non-sec}})\cdot E_{\text{dip}}^{\text{non-sec}} + E_{\text{dip}}^{\text{non-sec}\,2}}{2\pi\nu_{\text{T}}\omega_{\text{T}}}, \tag{S26}$$

$$E_{-\frac{1}{2},0}^{\text{non-sec}} = E_{-\frac{1}{2},0}^{\text{sec}} - \frac{\left|\langle-\frac{1}{2},+1|\hat{H}^{\text{non-sec}}|-\frac{1}{2},\,0\rangle\right|^2}{\omega_{\text{T}}2\pi\nu_{\text{T}}} + \frac{\left|\langle-\frac{1}{2},0|\hat{H}^{\text{non-sec}}|-\frac{1}{2},\,-1\rangle\right|^2}{2\pi\nu_{\text{T}}\omega_{\text{T}}} = 4\frac{E_{\text{ZFS}}^{\text{non-sec}}\cdot E_{\text{dip}}^{\text{non-sec}}}{2\pi\nu_{\text{T}}\omega_{\text{T}}}, \tag{S27}$$

$$E_{-\frac{1}{2},-1}^{\text{non-sec}} = E_{-\frac{1}{2},-1}^{\text{sec}} - \frac{\left|\langle-\frac{1}{2},0|\hat{H}^{\text{non-sec}}|-\frac{1}{2},\,-1\rangle\right|^2}{2\pi\nu_{\text{T}}\omega_{\text{T}}} = -\frac{|E_{\text{ZFS}}^{\text{non-sec}}|^2 + 2\text{Re}(E_{\text{ZFS}}^{\text{non-sec}})\cdot E_{\text{dip}}^{\text{non-sec}} + E_{\text{dip}}^{\text{non-sec}\,2}}{2\pi\nu_{\text{T}}\omega_{\text{T}}}. \tag{S28}$$

Here, Re stands for the real-part of a number. The LaserIMD frequencies can then be calculated as follows:

$$\omega_{+1}^{\text{non-sec}} = \left(E_{+\frac{1}{2},+1}^{\text{non-sec}} - E_{-\frac{1}{2},+1}^{\text{non-sec}}\right) - \left(E_{+\frac{1}{2},\text{dark}} - E_{-\frac{1}{2},\text{dark}}\right) = \left(3\cos(\beta_{\text{dip}})^2 - 1\right)\omega_{\text{d}} + \frac{4\text{Re}(E_{\text{ZFS}}^{\text{non-sec}})\cdot E_{\text{dip}}^{\text{non-sec}}}{2\pi\nu_{\text{T}}\omega_{\text{T}}}, \tag{S29}$$

$$\omega_{0}^{\text{non-sec}} = \left(E_{+\frac{1}{2},0}^{\text{non-sec}} - E_{-\frac{1}{2},0}^{\text{non-sec}}\right) - \left(E_{+\frac{1}{2},\text{dark}} - E_{-\frac{1}{2},\text{dark}}\right) = -\frac{8\text{Re}(E_{\text{ZFS}}^{\text{non-sec}})\cdot E_{\text{dip}}^{\text{non-sec}}}{2\pi\nu_{\text{T}}\omega_{\text{T}}}, \tag{S30}$$

$$\omega_{-1}^{\text{non-sec}} = \left(E_{+\frac{1}{2},-1}^{\text{non-sec}} - E_{-\frac{1}{2},-1}^{\text{non-sec}}\right) - \left(E_{+\frac{1}{2},\text{dark}} - E_{-\frac{1}{2},\text{dark}}\right) = -\left(3\cos(\beta_{\text{dip}})^2 - 1\right)\omega_{\text{dip}} + \frac{4\text{Re}(E_{\text{ZFS}}^{\text{non-sec}})\cdot E_{\text{dip}}^{\text{non-sec}}}{2\pi\nu_{\text{T}}\omega_{\text{T}}}. \tag{S31}$$

~~These expressions are equivalent to the ones in the main also presented.~~ Insertion of Eq. (S16) an (S17) for $E_{\text{ZFS}}^{\text{non-sec}}$ and $E_{\text{dip}}^{\text{non-sec}}$ gives the expressions of Eq. (21) –(23) of the main text.

The same corrections of the energy levels can be used to calculate the LiDEER frequencies:

$$\omega_{+\frac{1}{2}\to-\frac{1}{2},+1\leftrightarrow0}^{\text{non-sec}} = \left(E_{+\frac{1}{2},+1}^{\text{non-sec}} - E_{+\frac{1}{2},0}^{\text{non-sec}}\right) - \left(E_{-\frac{1}{2},+1}^{\text{non-sec}} - E_{-\frac{1}{2},0}^{\text{non-sec}}\right) = \left(3\cos(\beta_{\text{dip}})^2 - 1\right)\omega_{\text{dip}} + \frac{12\text{Re}(E_{\text{ZFS}}^{\text{non-sec}})\cdot E_{\text{dip}}^{\text{non-sec}}}{2\pi\nu_{\text{T}}\omega_{\text{T}}}, \tag{S32}$$

$$\omega_{+\frac{1}{2}\to-\frac{1}{2},+1\leftrightarrow0}^{\text{non-sec}} = \left(E_{+\frac{1}{2},+1}^{\text{non-sec}} - E_{+\frac{1}{2},0}^{\text{non-sec}}\right) - \left(E_{-\frac{1}{2},+1}^{\text{non-sec}} - E_{-\frac{1}{2},0}^{\text{non-sec}}\right) = -\left(3\cos(\beta_{\text{dip}})^2 - 1\right)\omega_{\text{dip}} + \frac{12\text{Re}(E_{\text{ZFS}}^{\text{non-sec}})\cdot E_{\text{dip}}^{\text{non-sec}}}{2\pi\nu_{\text{T}}\omega_{\text{T}}}, \tag{S33}$$

$$\omega_{+\frac{1}{2}\to-\frac{1}{2},0\leftrightarrow-1}^{\text{non-sec}} = \left(E_{+\frac{1}{2},+1}^{\text{non-sec}} - E_{+\frac{1}{2},0}^{\text{non-sec}}\right) - \left(E_{-\frac{1}{2},+1}^{\text{non-sec}} - E_{-\frac{1}{2},0}^{\text{non-sec}}\right) = \left(3\cos(\beta_{\text{dip}})^2 - 1\right)\omega_{\text{dip}} - \frac{12\text{Re}(E_{\text{ZFS}}^{\text{non-sec}})\cdot E_{\text{dip}}^{\text{non-sec}}}{2\pi\nu_{\text{T}}\omega_{\text{T}}}, \tag{S34}$$

$$\omega_{+\frac{1}{2}\to-\frac{1}{2},0\leftrightarrow-1}^{\text{non-sec}} = \left(E_{+\frac{1}{2},+1}^{\text{non-sec}} - E_{+\frac{1}{2},0}^{\text{non-sec}}\right) - \left(E_{-\frac{1}{2},+1}^{\text{non-sec}} - E_{-\frac{1}{2},0}^{\text{non-sec}}\right) = -\left(3\cos(\beta_{\text{dip}})^2 - 1\right)\omega_{\text{dip}} - \frac{12\text{Re}(H_{\text{ZFS}}^{\text{non-sec}})\cdot H_{\text{dip}}^{\text{non-sec}}}{2\pi\nu_{\text{T}}\omega_{\text{T}}}. \tag{S35}$$

5

## S2 Influence of the remaining non-secular terms
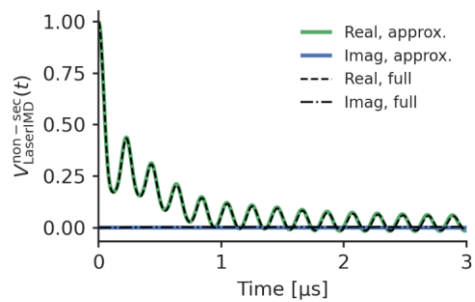
Figure S1: The dotted lines show a numerical calculation of a LaserIMD trace as a numerical simulation of the Liouville-von-Neumann equation with all terms in the Hamiltonian, the green and blue trace show the same trace calculated with the equations, derived in SI1. Both simulations used the values: $D = 1159$ MHz, $E= -238$ MHz, $P_x = 0.33$, $P_y = 0.41$, $P_z = 0.26$, $r = 2.2$ nm and $\omega_T \nu_T = 9.3$ GHz.

5

S3 Convergence of the integral

For the test-run, the following parameters were used: $D = 1159$ MHz, $E = -238$ MHz, $P_x = 0.33$, $P_y = 0.41$, $P_z = 0.26$, $r = 2.2$ nm and $\nu\omega_T = 9.3$ GHz. For the dipolar grid, the relative change was below 1 % when going from 100 to 200 grid points. In Figure S2 the convergence in dependence of the number of grid points for the transient label is shown. Whereas $V_{+1}^{\text{non}-\text{sec}}(t)$ and $V_{-1}^{\text{non}-\text{sec}}(t)$ have already converged when going from 100 to 200 points for the grid of the transient label, $V_{\text{LaserIMD}}^{\text{non}-\text{sec}}(t)$ and $V_0^{\text{non}-\text{sec}}(t)$ converge much slower. Particularly $V_0^{\text{non}-\text{sec}}(t)$ requires 12800 points until it is sufficiently converged. Figure S3 shows how $V_0^{\text{non}-\text{sec}}(t)$ changes when the number of grid points is increased.
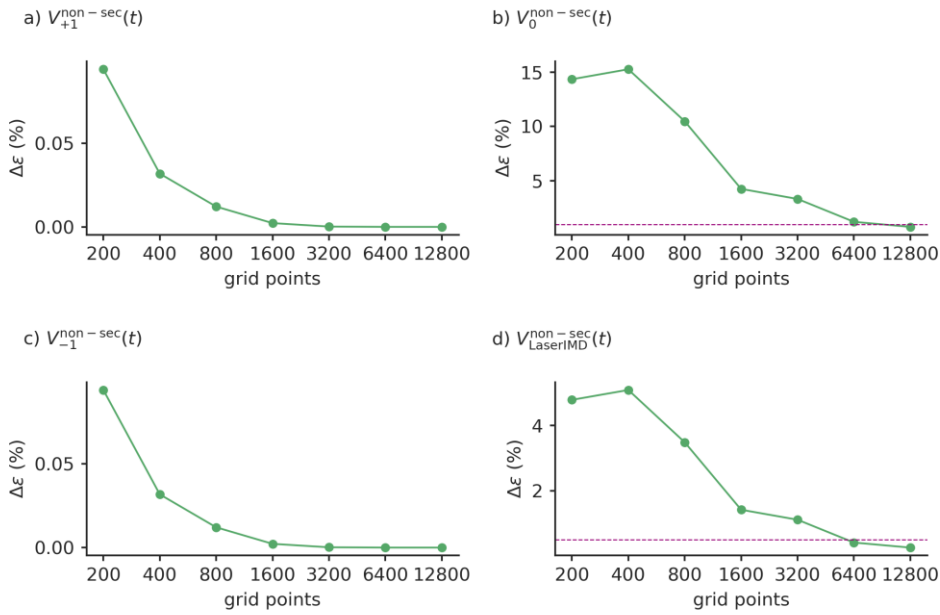
Figure S2: The relative change of the numerically calculated integral as a function of increasing grid points for a) $V_{+1}^{\text{non}-\text{sec}}(t)$, b) $V_0^{\text{non}-\text{sec}}(t)$, c) $V_{-1}^{\text{non}-\text{sec}}(t)$, d) $V_{\text{LaserIMD}}^{\text{non}-\text{sec}}(t) = V_{+1}^{\text{non}-\text{sec}}(t) + V_0^{\text{non}-\text{sec}}(t) + V_{-1}^{\text{non}-\text{sec}}(t)$. The parameters are set to $D = 1159$ MHz, $E = -238$ MHz, $P_x = 0.33$, $P_y = 0.41$, $P_z = 0.26$, $r = 2.2$ nm and $\nu\omega_T = 9.3$ GHz. The grid for the dipolar vector contained 200 points. The 1 % line is drawn in b) and d), for the a) and c) it is outside the boundaries of the plot. The relative change at 200 points refers to the signals that were calculated with 100 pts.
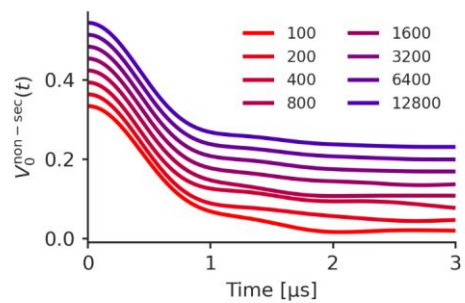
Figure S3: The numerical integration for $V_0^{non-sec}(t)$ for different number of points for the grid of the triplet. $D = 1159$ MHz, E= -238 MHz, $P_x = 0.33$, $P_y = 0.41$, $P_z = 0.26$, r = 2.2 nm and $\nu\omega_T = 9.3$ GHz. The grid for the dipolar vector contained 200 points. The traces are shifted by 0.03 for better visibility.

5

10

S4 LaserIMD simulations for different Zeeman frequencies
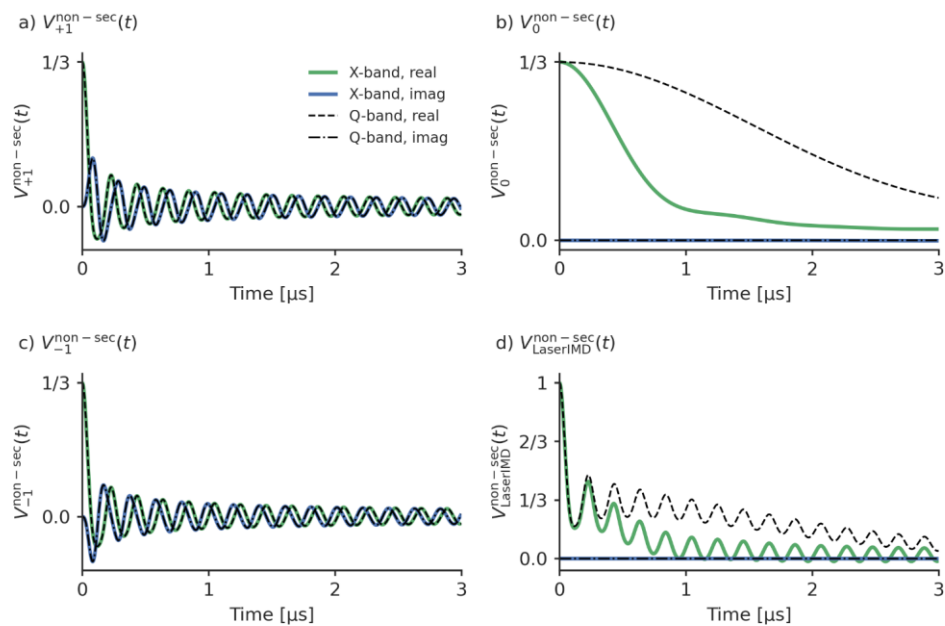
Figure S4: Simulations with TPP as transient spin label and $r = 2.2$ nm and $\nu_T = 34$ GHz (green and blue) and $\nu_T = 9.3$ GHz (black dashed lines). a) $V_{+1}^{non-sec}(t)$, b) $V_0^{non-sec}(t)$, c) $V_{-1}^{non-sec}(t)$, d) $V_{LaserIMD}^{non-sec}(t) = V_{+1}^{non-sec}(t) + V_0^{non-sec}(t) + V_{-1}^{non-sec}(t)$.

S5 LaserIMD simulations for different ZFS values
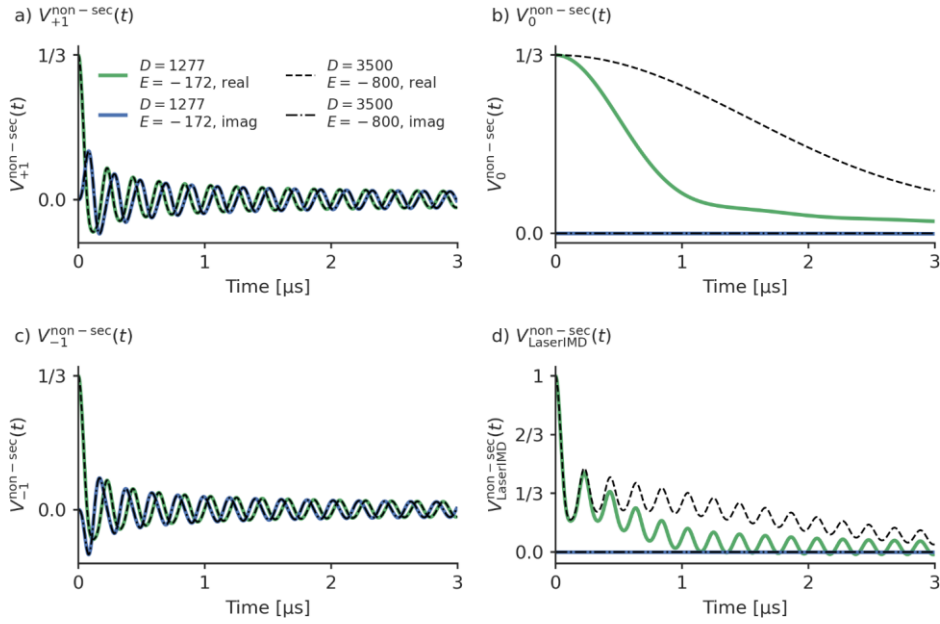
Figure S5: Simulations with different ZFS values with the following parameters: $P_x = 0.33$, $P_y = 0.41$, $P_z = 0.26$, $r = 2.2$ nm, $\omega\nu_T = 9.3$ GHz and $D = 1227$ MHz, E= -172 MHz (green and blue) and $D = 3500$ MHz, E= -800 MHz (black dashed lines) a) $V_{+1}^{non-sec}(t)$, b) $V_0^{non-sec}(t)$, c) $V_{-1}^{non-sec}(t)$, d) $V_{LaserIMD}^{non-sec}(t) = V_{+1}^{non-sec}(t) + V_0^{non-sec}(t) + V_{-1}^{non-sec}(t)$. The ZFS values in the legend are given in MHz.

S6 LaserIMD simulations for different distances

a) $V^{non-sec}_{+1}(t)$

b) $V^{non-sec}_{0}(t)$

c) $V^{non-sec}_{-1}(t)$

d) $V^{non-sec}_{LaserIMD}(t)$
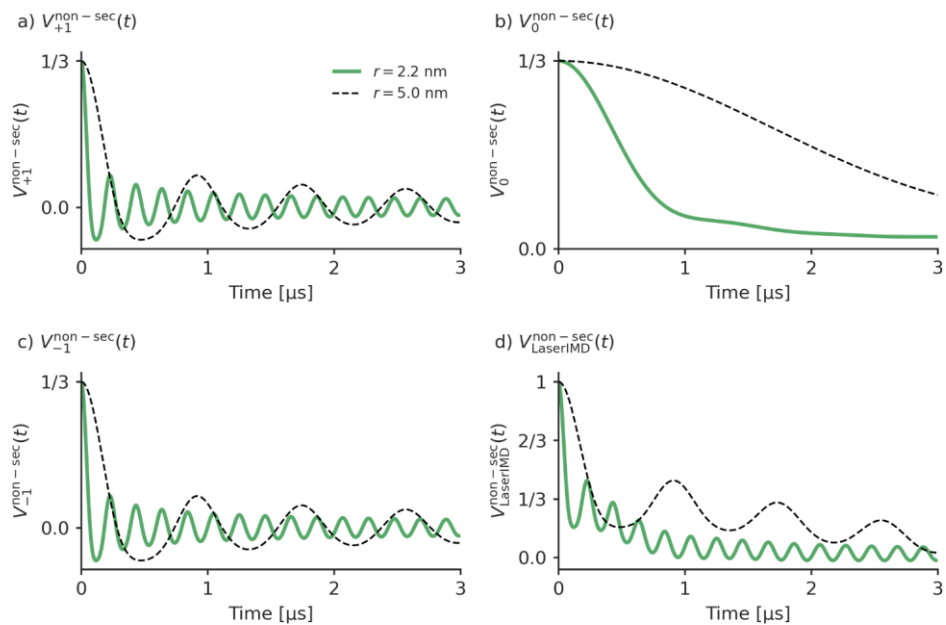
Figure S6: Simulations with TPP as transient spin label and $\nu\omega_T = 9.3$ GHz and $r = 2.2$ nm (green) and $r = 5.0$ nm (dashed black lines). a) $V^{non-sec}_{+1}(t)$, b) $V^{non-sec}_{0}(t)$, c) $V^{non-sec}_{-1}(t)$, d) $V^{non-sec}_{LaserIMD}(t) = V^{non-sec}_{+1}(t) + V^{non-sec}_{0}(t) + V^{non-sec}_{-1}(t)$.

5

S7 Calculation of distance distributions with Tikhonov regularization

The distance distributions of simulated and experimentally recorded traces were obtained with the package *DeerLab* (version 0.13.2) (Fábregas Ibáñez et al., 2020) in *Python* 3.9. As a first step, a phase- and zero-time correction was done. The traces were then fitted with Tikhonov regularization in a one-step procedure, where the background and distance distribution are not
5   fitted subsequently but in one step. The dipolar-kernel of a four-pulse DEER experiment $K_{\text{DEER}}(t,r)$ was used and the background function was assumed to have the shape of an exponential decay. The regularization parameter was chosen according to the Akaiki information criterion (Edwards and Stoll, 2018). The validation was performed with bootstrapping by generating 1000 sampled with artificial noise that were subsequently analyzed. The error was then calculated as the 95 % confidence interval.

10

S8 LiDEER simulations

The time-domain simulations of the LiDEER pulse sequence laser pulse – DAF – $\pi/2$ – τ_1 – π – t – π – pump – $(\tau_2 - t)$ – π – τ_{delay} – echo (Di Valentin et al., 2014) were performed with the package *Spinach* (version 2.6.5625) (Hogben et al., 2011) in MATLAB (R2021b). *Spinach* calculates a numerical solution of the Liouville-von-Neumann equation by density matrix

5   propagation. The spin system consisted of a photoexcited transient spin label in its triplet state and a permanent spin label that was included as a doublet spin. For the transient spin label we chose TPP or a spin system with a larger ZFS ($D = 3500$ MHz, $E = -800$ MHz) and simulations in X- and Q-band were performed. No additional hyperfine interactions were included. The distance between the two spins was set to $r = 2.2$ nm. The full spin Hamiltonian including all terms from Eq. 10 from the main text was used, and the simulations were performed in the laboratory frame. The starting density matrix was obtained as

10   the Kronecker product of the spin polarized state of the transient label which was calculated according to (Williams et al., 2020) and the equilibrated state of the permanent spin label ($T = 30$ K). All operators and states were treated in Liouville representation with spherical tensors. The effects of the microwave pulses with a finite width and power were calculated by stepwise propagation in the time-domain. The power of the microwave pulses was calculated such that the flip angles corresponds to the required $\pi/2$ or π and for the transient spin label, the effect of the higher transition dipole moment was

15   considered. The observer frequency was set to be either be on-resonance to the Y^+ canonical peak or it was set to a part of the spectrum between the X^+ and the Y^+ peak where all canonical orientations are off-resonance. The pump frequency was set to the frequency of the permanent radical (see Figure S7). The signal was obtained by summing over the echo in the range of the full-width half maximum. This integration window and the exact time delay τ_{delay} of the echo were determined manually by the simulation of the echo. The powder average was done by summing over the different orientations for the transient spin

20   label and the dipolar coupling vector. For that, the same grids as for the LaserIMD simulations were used. As the permanent spin label does not contain any anisotropic interaction, no powder averaging was performed for it. The source code for the LiDEER simulations can be downloaded at https://github.com/andreas-scherer/LiDEER_simulations.git.

13
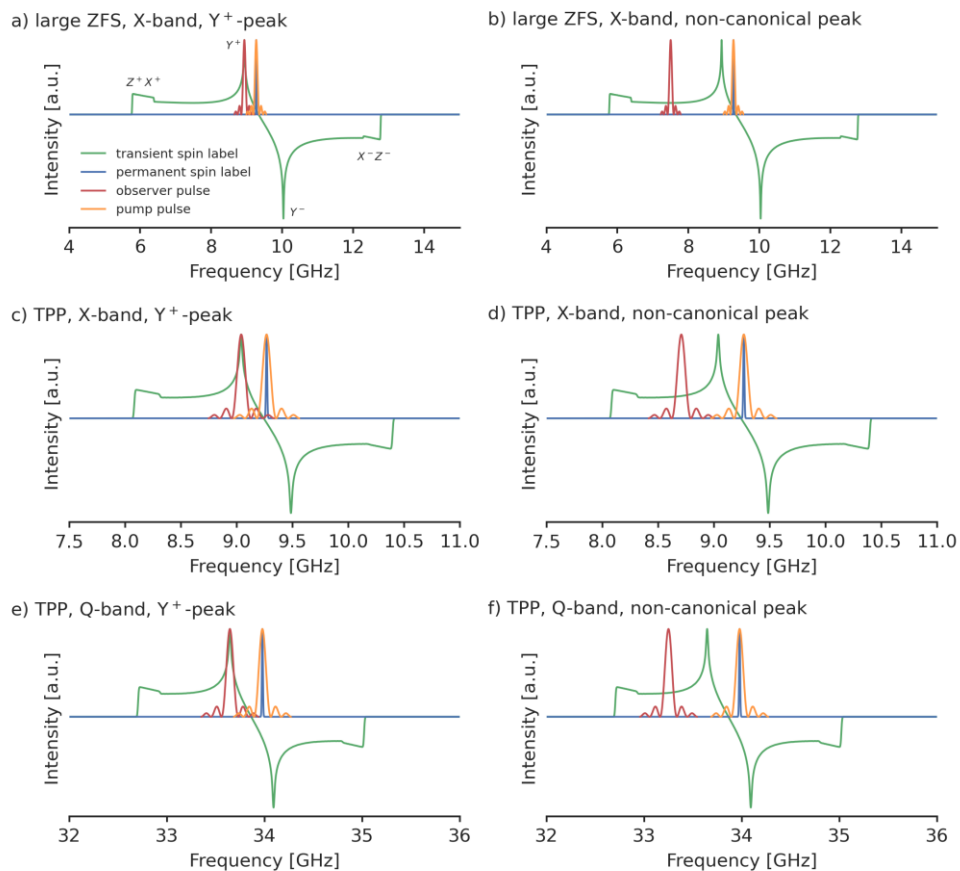
Figure S7: The EPR spectra of the transient spin label (green) with the canonical peaks marked in a), the permanent spin label (blue), the excitation profile of the observer π-pulse (red) and the pump π-pulse (orange) that were used in the LiDEER simulations. a) and b) $D = 3500$ MHz, $E = -800$ MHz, $P_x = 0.33$, $P_y = 0.41$ and $P_z = 0.26$ in X-band; c) and d) TPP as transient spin label in X-band; e) and f) TPP as transient spin label in Q-band. a), c) and e) the observer pulse is positioned on the Y^+-peak. b), d) and f) the observer pulse is positioned off-resonance to all canonical orientations. The EPR spectra and excitation profiles were simulated with *easyspin* (Stoll and Schweiger, 2006). The relative intensities of the EPR spectra of the transient and permanent spin labels do not reflect their actual intensities. They are both normalized for better visibility.

Table S1: The details of the time-domain LiDEER simulations.

	Y⁺ orientation			Non-canonical orientation		
	Large ZFS (X-band)	TPP (X-band)	TPP (Q-band)	Large ZFS (X-band)	TPP (X-band)	TPP (Q-band)
g-value (permanent spin label)	2			2		
g-value (transient spin label)	2.00687			2.00687		
D / E [MHz]	3500/ -800	1159/ -238		3500/ -800	1159/ -238	
$P_x / P_y / P_z$	0.33/ 0.41/ 0.26			0.33/ 0.41/ 0.26		
Magnetic field [T]	0.33		1.2097	0.33		1.2097
Observer frequency [GHz]	8.934	9.042	33.646464	7.500	8.709	3.250
Pump frequency [GHz]	9.269		33.979	9.269		33.979
Observer $\pi/2$-pulse length [ns]	10			20		
Observer π-pulse length [ns]	20			20		
Pump π-pulse length [ns]	10			10		
Observer $\pi/2$-pulse power [MHz]	17.68			17.68		
Observer π-pulse power [MHz]	17.68			17.68		
Pump π-pulse power [MHz]	50			50		
τ_1 [μs]	0.1			0.1		
τ_2 [μs]	2.1			2.1		
Time step $\Delta\tau$ [ns]	8			8		

S9 Results of the LiDEER simulations on a non-canonical orientation
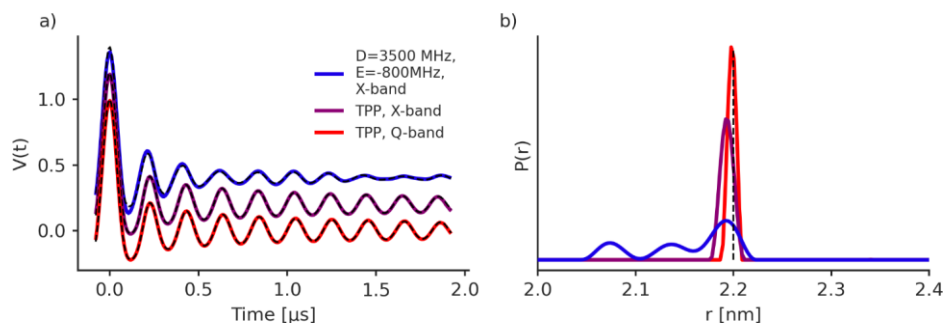
Figure S8: a) Numerical simulation of LiDEER with the observer pulse placed off-resonance to all canonical peaks of the EPR spectrum of the transient spin label at different frequency bands and with different ZFS. The traces are shifted by 0.2 for better visibility. For Q-band and TPP the magnetic field was set to 1.2097 T and the observer frequency to 33.250 GHz, for X-band the magnetic field was set to 0.33 T, which for TPP corresponds to an observer frequency of 8.709 GHz and for a ZFS with D = 3500 MHz and E = −800 MHz to an observer frequency of 7.500 GHz. The position of the observer and pump pulse with respect to the EPR spectrum is shown in Fig. S7b, d and f. The further parameters are $P_x = 0.33$, $P_y = 0.41$, $P_z = 0.26$ and r = 2.2 n m. The numerical simulations were fitted with Tikhonov regularization and a dipolar kernel that does not take non-secular interactions into account. The fits are shown as black line and b) shows the corresponding distance distribution. The true distance of r = 2.2 nm is plotted as dotted black line.

16

S10 EPR experiments

<u>Sample preparation</u>

All solvents were purchased from Merck and used without further purification. The peptides TPP-pAA$_5$-NO• and TPP-pAA$_{10}$-NO• were purchased from Biosynthan as freeze-dried powder and used without further purification. They were dissolved in 98/2 MeOD$_4$/ D$_2$O [vol.%]. The TPP-pAA$_5$-NO• sample had a concentration of 10 μM and the TPP-pAA$_{10}$-NO• sample had a concentration of 50 μM. The samples were loaded in a 3mm outer-diameter quartz-tube. A sample volume of 10 μl (filling height 5 mm) was used in order to maintain a uniform excitation throughout the sample. Prior to shock-freezing in liquid nitrogen, these samples were also degassed by three consecutive freeze-pump-thaw cycles for oxygen removal. All samples were measured at a temperature of 30 K with a repetition time of 50 ms. The laser excitation took place at a wavelength of 510 nm.

<u>The laser system</u>

Light excitation was achieved with a tunable diode pumped Nd:YAG laser system NT230-50-ATTN2-FC (Ekspla, Vilnius, Lithuania) comprising a pump laser, second and third harmonic generators and an optical parametric oscillator (OPO). Unless stated otherwise, the system was operated with pulse energies of ≈ 3.5 mJ (measured before the laser fiber, standard deviation ≈ 0.2 μJ). As the fibre has a transmission of approximately 40 %, this results in an energy after the fiber of ≈ 1.4 mJ. Triggering was performed by means of the spectrometer's pulse PatternJet (Q-band pulsed EPR measurements) or an external pulse generator (time resolved EPR measurements). The light was coupled into the resonator using a quartz glass fiber (1 mm core, Pigtail WF 1000/ 1100/ 1600 T, CeramOptec GmbH, Bonn, Germany), with its end adjusted to a height of 1 cm above the sample surface.

<u>X-band measurements</u>

X-band EPR spectra were recorded on a Bruker Elexsys E580 spectrometer (Bruker Biospin) and a 1 kW amplifier in an overcoupled ER4118X-MS3 resonator (Bruker Biospin). It was critically coupled to a Q-value of ≈ 900-2000. The temperature was controlled with a CF935 helium gas flow system (Oxford instruments) controlled by an ITC (Oxford Instruments).

<u>Q-band measurements</u>

Q-band measurements were performed on a Bruker Elexsys E580 spectrometer equipped with a SpinJet-AWG unit (Bruker Biospin, Rheinstetten, Germany) and a 150 W pulsed TWT amplifier (Applied Systems Engineering, Fort Worth, USA). A commercial Q-band resonator from Bruker Biospin (ER5106QT-2) was used for all pulsed EPR measurements. It was overcoupled to a Q-factor of ≈ 200. The temperature was maintained with the EPR Flexline helium recirculation system (CE-FLEX-4K-0110, Bruker Biospin, ColdEdge Technologies), comprising a cold head (expander, SRDK-408D2) and a F-70H compressor (both SHI cryogenics, Tokyo, Japan), controlled by an Oxford Instruments Mercury ITC. Echo signals were

17

detected in integrator mode with a video bandwidth of 20 MHz. The integrator gate was set symmetrically around the echo with a length that equals the full width at half maximum of the echo.

LiDEER

LiDEER measurements were performed in Q-band with the pulse-sequence: laser pulse – DAF – $\pi/2 - \tau_1 - \pi - t - \pi_{pump} -$
5 ~~pump~~ $- (\tau_1 + \tau_2 - t) - \pi - \tau_2$ – echo (Di Valentin et al., 2014) (note that due to technical reasons the definitions of some of the parameters in the LiDEER pulse-sequence for the experiments are different to those that were used for the time-domain simulations). The delay-after-flash (DAF) was set to 500 ns and τ_1 to 400 ns. Nuclear modulation averaging was performed by varying the τ_1 time in 8 steps with $\Delta\tau_1 = 16$ ns. Phase cycling was performed with the 8-step scheme ((x) [x] xp x) as proposed by (Tait and Stoll, 2016). The observer frequency was set to 34.00 GHz and the pump frequency to 33.84 GHz. All pulses
10 were rectangular pulses. All further parameters can be found in Table S2.

Table S2: The parameters for the LiDEER measurements.

	TPP-pAA$_5$-NO$^\bullet$	TPP-pAA$_{10}$-NO$^\bullet$
Magnetic field [T]	1.2045	1.2052
Observer π-pulse length [ns]	20	20
Pump π-pulse length [ns]	48	52
τ_1 [μs]	0.4	0.4
Trace length τ_2 [μs]	2.6	6.1
Time step $\Delta\tau$ [ns]	8	16
Microwave attenuation [dB]	0	0
Shots per point	1	1
Number of averages	74	65
Video gain [dB]	21	21

LaserIMD

LaserIMD experiments were performed with the pulse-sequence $\pi/2 - \tau - \pi - t$ - laser pulse - $(\tau\text{-}t)$ - echo reported by (Hintze et al., 2016). A 2-step phase cycle was implemented for baseline correction. All pulses were rectangular pulses. The magnetic
15 field was set to the maximum of the nitroxide EPR spectrum at the corresponding microwave frequency, All further parameters can be found in Table S3.

18

Table S3: The parameters for the LaserIMD measurements.

	TPP-pAA$_5$-NO$\bullet$		TPP-pAA$_{10}$-NO$\bullet$	
Microwave frequency [GHz]	9.28 (X-band)	34.0 (Q-band)	9.31 (X-band)	34.0 (Q-band)
Magnetic field [T]	0.3304	1.2097	0.3314	1.2097
π-pulse length [ns]	24	28	24	28
Trace length τ [µs]	1.4	2.5	3.2	6.0
Time step $\Delta\tau$ [ns]	8	8	16	16
Microwave attenuation [dB]	13	0	11	0
Shots per point	10	10	10	10
Number of averages	483	146	346	177
Video gain [dB]	50	27	50	36

reLaserIMD

For the determination for the zero-time as described in (Scherer et al., 2022) a refocused LaserIMD (reLaserIMD) trace was
5   recorded in X- and Q-band with TPP-pAA$_5$-NO$\bullet$. As the zero-time does not depend on the type of sample, the thus determined zero-time was also used for the peptide TPP-pAA$_{10}$-NO$\bullet$. We used the shorter peptide for zero-time determination, because due to the faster dipolar oscillations it can be determined more precisely. We used the pulse-sequence $\pi/2 - \tau_1 - \pi - t$ - laser pulse - $(\tau_1 + \tau_2 - t) - \tau_2 - \pi$ - echo as reported by (Dal Farra et al., 2019). A 2-step phase cycle was implemented for baseline correction. All pulses were rectangular pulses. The magnetic field was set to the maximum of the nitroxide EPR spectrum at
10   the corresponding microwave frequency. All further parameters can be found in Table S4.

15

19

Table S4: The parameters for the reLaserIMD measurements.

	TPP-pAA$_5$-NO•	
Microwave frequency [GHz]	9.28 (X-band)	34.0 (Q-band)
Magnetic field [T]	0.3304	1.2097
π-pulse length [ns]	24	28
τ_1 [µs]	0.4	0.8
Trace length τ_2[µs]	0.4	1.0
Time step $\Delta\tau$ [ns]	8	8
Microwave attenuation [dB]	13	0
Shots per point	10	10
Number of averages	10	219
Video gain [dB]	50	27

S11 Analysis of the experimental LaserIMD data
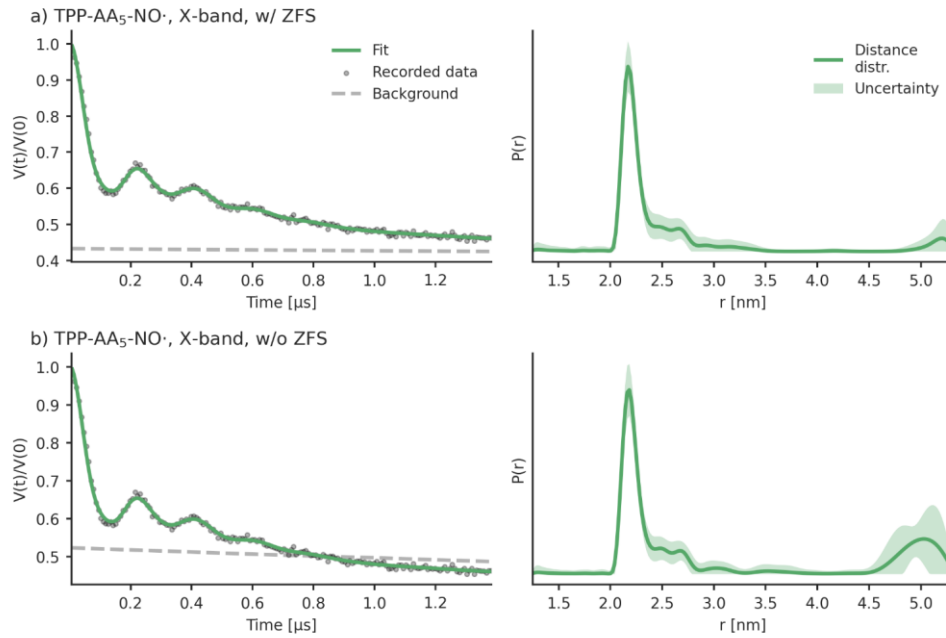
Figure S9: Experimental LaserIMD data of TPP-pAA$_5$-NO• recorded in X-band at 30 K in MeOD/D$_2$O (98/2 vol.%). a) Analyzed with a kernel that includes the ZFS and b) Analyzed with a kernel that ignores the ZFS. The raw data are depicted on the left side as grey dots with the fits as green line, the background fit is depicted as dashed grey line. The distance distributions obtained with Tikhonov regularization (Fábregas Ibáñez et al., 2020) is shown on the right side. The shaded areas correspond to the 95% confidence intervals that were obtained with bootstrapping.
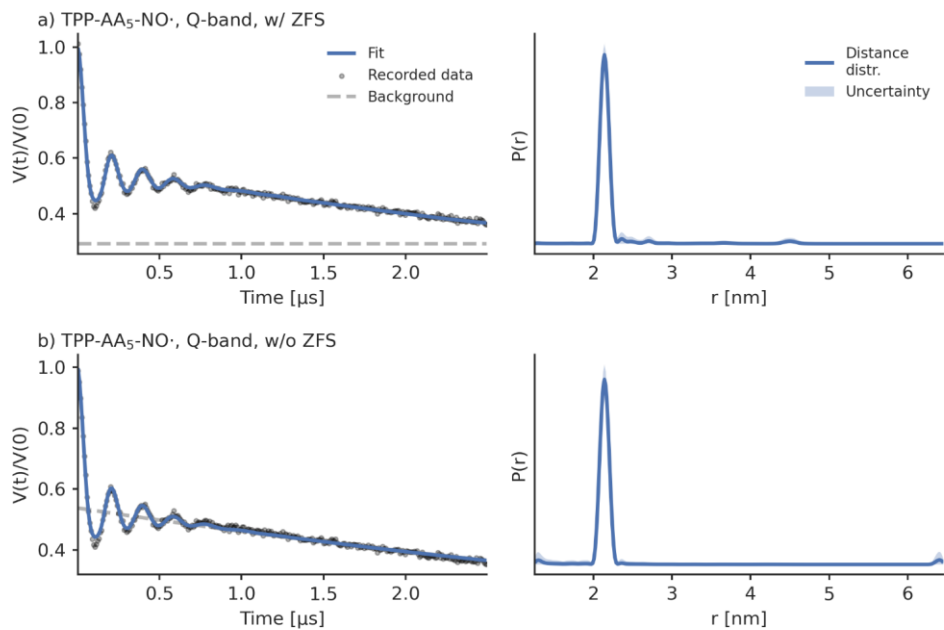
Figure S10: Experimental LaserIMD data of TPP-pAA$_5$-NO• recorded in Q-band at 30 K in MeOD/D$_2$O (98/2 vol.%). a) Analyzed with a kernel that includes the ZFS and b) Analyzed with a kernel that ignores the ZFS. The raw data are depicted on the left side as grey dots with the fits as blue line, the background fit is depicted as dashed grey line. The distance distributions obtained with Tikhonov regularization (Fábregas Ibáñez et al., 2020) is shown on the right side. The shaded areas correspond to the 95% confidence intervals that were obtained with bootstrapping.

a) TPP-AA$_{10}$-NO·, X-band, w/ ZFS

b) TPP-AA$_{10}$-NO·, X-band, w/o ZFS
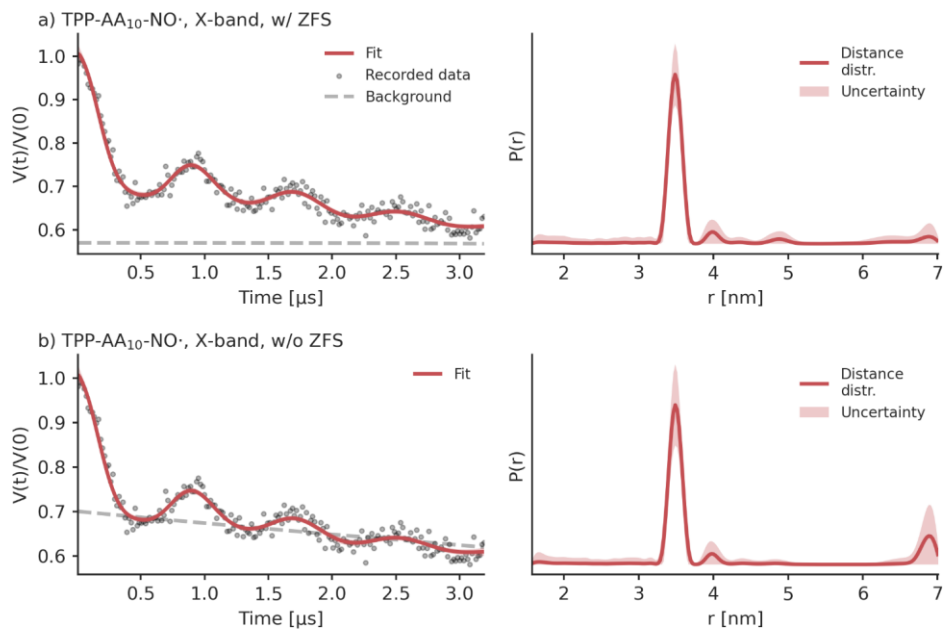
Figure S11: Experimental LaserIMD data of TPP-pAA$_{10}$-NO• recorded in X-band at 30 K in MeOD/D$_2$O (98/2 vol.%). a) Analyzed with a kernel that includes the ZFS and b) Analyzed with a kernel that ignores the ZFS. The raw data are depicted on the left side as grey dots with the fits as red line, the background fit is depicted as dashed grey line. The distance distributions obtained with Tikhonov regularization (Fábregas Ibáñez et al., 2020) is shown on the right side. The shaded areas correspond to the 95% confidence intervals that were obtained with bootstrapping.

5

Figure S13: A comparison of the distance distributions that were obtained by analyzing the experimental LaserIMD data with a kernel that includes the ZFS (**coloured lines) and** with a kernel that ignores the FS (black **lines). a)** TPP-pAA$_5$-NO• in X-band. b) TPP-pAA$_5$-NO• in Q band. **c)** TPP-pAA$_{10}$-NO• in X-band. **a)** TPP-pAA$_{10}$-NO• in Q-band.

Table S5: Background decay rates and modulation depths as obtained by the analysis of the LaserIMD data of TPP-pAA$_5$-NO•.

	X-band		Q-band	
	w/ ZFS	w/o ZFS	w/ ZFS	w/o ZFS
Background decay rate [μs^{-1}]	0.0 (0.0, 0.2)	0.1 (0.0, 0.3)	0.000 (0.003, 0.000)	0.33 (0.27, 0.36)
Modulation depth [%]	57 (52, 59)	48 (43, 52)	71 (70, 72)	46 (45, 49)

Table S6: Background decay rates and modulation depths as obtained by the analysis of the LaserIMD data of TPP-pAA$_{10}$-NO•.

	X-band		Q-band	
	w/ ZFS	w/o ZFS	w/ ZFS	w/o ZFS
Background decay rate [μs^{-1}]	0.00 (0.00, 0.05)	0.13 (0.01, 0.28)	0.03 (0.01, 0.04)	0.09 (0.07, 0.11)
Modulation depth [%]	43 (40, 45)	31 (25, 36)	26 (25, 27)	17 (16, 18)

S12 References

Abragam, A. and Bleaney, B.: Electron paramagnetic resonance of transition ions, Oxford University Press, 2012.

Blank, A. and Levanon, H.: Triplet line shape simulation in continuous wave electron paramagnetic resonance experiments, Concepts Magn. Reson. Part A, 25A, 18–39, https://doi.org/10.1002/cmr.a.20030, 2005.

5   Dal Farra, M. G., Richert, S., Martin, C., Larminie, C., Gobbo, M., Bergantino, E., Timmel, C. R., Bowen, A. M., and Di Valentin, M.: Light-induced pulsed EPR dipolar spectroscopy on a paradigmatic Hemeprotein, ChemPhysChem, 0, https://doi.org/10.1002/cphc.201900139, 2019.

Di Valentin, M., Albertini, M., Zurlo, E., Gobbo, M., and Carbonera, D.: Porphyrin Triplet State as a Potential Spin Label for Nanometer Distance Measurements by PELDOR Spectroscopy, J. Am. Chem. Soc., 136, 6582–6585, 10   https://doi.org/10.1021/ja502615n, 2014.

Edwards, T. H. and Stoll, S.: Optimal Tikhonov regularization for DEER spectroscopy, J. Magn. Reson., 288, 58–68, https://doi.org/10.1016/j.jmr.2018.01.021, 2018.

Fábregas Ibáñez, L., Jeschke, G., and Stoll, S.: DeerLab: A comprehensive toolbox for analyzing dipolar EPR spectroscopy data, Magn. Reson. Discuss., 2020, 1–28, https://doi.org/10.5194/mr-2020-13, 2020.

15   Hintze, C., Bücker, D., Domingo Köhler, S., Jeschke, G., and Drescher, M.: Laser-Induced Magnetic Dipole Spectroscopy, J. Phys. Chem. Lett., 7, 2204–2209, https://doi.org/10.1021/acs.jpclett.6b00765, 2016.

Hogben, H. J., Krzystyniak, M., Charnock, G. T. P., Hore, P. J., and Kuprov, I.: Spinach – A software library for simulation of spin dynamics in large spin systems, J. Magn. Reson., 208, 179–194, https://doi.org/10.1016/j.jmr.2010.11.008, 2011.

Scherer, A., Yao, X., Qi, M., Wiedmaier, M., Godt, A., and Drescher, M.: Increasing the Modulation Depth of Gd(III)-Based 20   Pulsed Dipolar EPR Spectroscopy (PDS) with Porphyrin-Gd(III) Laser-Induced Magnetic Dipole Spectroscopy, J. Phys. Chem. Lett., 13, 10958–10964, https://doi.org/10.1021/acs.jpclett.2c02138, 2022.

Stoll, S. and Schweiger, A.: EasySpin, a comprehensive software package for spectral simulation and analysis in EPR, J. Magn. Reson., 178, 42–55, https://doi.org/10.1016/j.jmr.2005.08.013, 2006.

Tait, C. E. and Stoll, S.: Coherent pump pulses in Double Electron Electron Resonance spectroscopy, Phys. Chem. Chem. 25   Phys., 18, 18470–18485, https://doi.org/10.1039/C6CP03555H, 2016.

Williams, L., Tischlik, S., Scherer, A., Fischer, J. W. A., and Drescher, M.: Site-directed attachment of photoexcitable spin labels for light-induced pulsed dipolar spectroscopy, Chem. Commun., 56, 14669–14672, https://doi.org/10.1039/D0CC03101A, 2020.